Theorical and experimental study of plasmonic metamaterials for infrared application

Fatima Omeis

UNIVERSITÉ CLERMONT AUVERGNE
U.F.R. Science et Technologie

THÉSE

présentée pour obtenir le grade de

DOCTEUR D'UNIVERSITÉ
SPÉCIALITÉ: PHYSIQUE

Soutenue publiquement le 15 Septembre 2017 par

Fatima OMEIS
Master Nanostructures et Nanophotonique

Theoretical and experimental study of plasmonic metamaterials for infrared applications

Jury:

Beatrice Dagens	Dr. Université Paris Sud	Présidente
Nathalie Destouches	Prof. Université Saint-Étienne	Rapporteur
Olivier Gauthier Lafaye	Dr. LAAS-CNRS, Toulouse	Rapporteur
Emmanuel Centeno	Prof. Université Clermont Auvergne	Directeur
Thierry Taliercio	Prof. Université Montpellier	Co-directeur
Rafik Smaali	MCF Université Clermont Auvergne	Co-directeur

"*Physics is not the most important thing, love is.*"

Richard Feynman

Prologue

What happens when light meets matter? There is always an interaction. Sometimes these interactions are visible to our naked eye, others are not. This depend on the level of this interaction and the way of "observing" its physical influences. So understanding what light is and especially its way of interacting with material is a great treasure for new applications and a demanding criterion for the underlying physical theories.

Contents

Introduction

Since the first prediction of the existence of surface plasmons in 1957 by Rufus Ritchie [1], they have attracted exceptional attention because of their fascinating properties and their applications in many areas ranging from biological sensing, imaging, and biomedicine through photovoltaic, thermal emitters, and data storage. Plasmonic behavior originates from the coupling of an electromagnetic field and electrons leading to a wave propagating along a metal-dielectric interface or localized one metallic particles. The interest of plasmonics lies on the subwavelength confinement of the electromagnetic waves and the strong enhancement of the electric field around the metallic objects.

Usually, surface plasmon or localized plasmonic modes are excited with visible light (450nm-850nm) since noble metals like gold or silver are used to realized the plasmonic structures. But extending plasmonic properties to the infrared and THz spectra can benefit a lot of applications such of imagery or sensing domains. However, this extension demand to realize the adequate materials having metallic behavior at these frequencies and to properly design the structures. In this thesis, we address this issue by considering two approaches. First we propose plasmonic structures made up of highly doped semiconductor that allows the observation of the plasmonic resonances in the infrared and THz ranges. We also synthesize effective electromagnetic properties by using hyperbolic metamaterials. In the second approach, we propose a metasurface that overcomes the material limitations and efficiently absorbs electromagnetic radiations at any range of wavelengths.

In Chapter 1, we provide a brief introduction to plasmonics and the main principles. Then we shed the light on the search of better plasmonic materials to ameliorate the functioning of these structures. In this sense, we introduce the highly doped semiconductor as a functioning material in the THz range, which include a lot of interesting applications. Finally, we state the great

impact of bringing both plasmonics and metamaterials together in order to benefit from them in wide range of disciplines and frequencies.

In Chapter 2, we numerically and experimentally explore the plasmonic properties in the spectral range between $25 - 40\mu m$ ($12 - 7.5$ THz) of metal-insulator-metal (MIM) antennas made of highly Si-doped semiconductor(HDSC) InAsSb. We demonstrate that these MIM antennas sustain a gap plasmon mode that is responsible for high light absorption. By tracking this peculiar plasmonic signature for various antennas' width, we prove that Si-doped InAsSb microstructures realized on large areas by laser lithography and wet etching process is a low cost, reproducible and readily CMOS compatible approach.

In Chapter 3, we propose the concept of hyperbolic wires that overcomes the actual limitation of metal-insulator-metal (MIM) patch antennas in terms of electromagnetic confinement and efficiency. The use of hyperbolic metamaterials allows one to realize miniaturized resonators sustaining bulk plasmon polaritons squeezed to only one-hundredth of the wavelength. Beyond this tenfold size reduction compared to MIM antennas, we propose a model allowing one to scale the resonant frequencies of hyperbolic wires over a broad spectral range by controlling the filling ratio in metal and dielectric.

In Chapter 4, we propose a design for an universal absorber, characterized by a resonance frequency that can be tuned from visible to microwave frequencies independently of the choice of the metal and the dielectrics involved. An almost perfect absorption up to 99.8% is demonstrated at resonance for all polarization states of light and for a very wide angular aperture. These properties originate from a magnetic Fabry-Perot mode that is confined in a dielectric spacer of $\lambda/100$ thickness by a metamaterial layer and a mirror. An extraordinary large funnelling through nano-slits explains how light can be trapped in the structure. Simple scaling laws can be used as a recipe to design ultra-thin perfect absorbers whatever the materials and the desired resonance wavelength, making our design truly universal.

Chapter 1

Plasmonics and metamaterials

1.1 What is Plasmonics

The term 'plasmonics' is derived from plasmons quanta associated with collective longitudinal excitation of a conductive electron gas in a metals. The study of Plasmonics is a branch of Nanophotonics, it explores how electromagnetic fields can be confined over dimensions on the order of or smaller than the wavelength. It is based on the interaction processes between electromagnetic (EM) radiation and conduction electrons at metallic interfaces or in small metallic nanostructures, leading to an enhanced optical near field of sub-wavelength dimension far beyond the diffraction limit. Normally, surface plasmons are excited within or near the visible but it can be extended to the infrared regions. They are also well involved in the behavior of metamaterials constructed from deep subwavelength metallic features, producing unusual macroscopic properties, such as negative refractive index, and permittivity or near-zero permeability. The interaction of metals with EM field can be understood using the classical Maxwell's equations even for structures that have a size of few nanometers:

$$\begin{aligned}
\nabla \cdot \vec{D} &= \rho_{ext} && \text{electric charge is the source of the electric field} \\
\nabla \cdot \vec{B} &= 0 && \text{there are no source of magnetic field} \\
\nabla \times \vec{E} &= -\frac{\partial \vec{B}}{\partial t} && \text{change of B-field with time leads to a rotating E-field} \\
\nabla \times \vec{H} &= J_{ext} + \frac{\partial \vec{D}}{\partial t} && \text{electric currents give rise to rotating magnetizing field}
\end{aligned} \tag{1.1}$$

In these equation there are four macroscopic fields, $\vec{D}$ the dielectric displacements, $\vec{E}$ the electric field, $\vec{H}$ the magnetic field and $\vec{B}$ the magnetic flux density. In addition ρ_{ext} is the external charge density, while J_{ext} is the external current density.

1.1.1 Drude model

The electric permittivity $\varepsilon(\omega)$ is one of the main parameters that gives us information about the response of a material shined by an electromagnetic wave. For metals, this electrical property is described by the Drude model that was developed at the turn of the 20th century by Paul Drude [2]. Few years after J.J Thompson discovers the electron in 1897. It pre-dates the quantum theory, but still can tell us a lot about electron in metals. This model is based on the kinetic theory of electrons in a metal which assumes that the material has a non-interacting electron gas. It was constructed in order to explain the transport properties of conduction electron in metals, conductive oxides, and highly doped semiconductors. Since the conduction electrons are considered to be free, Drude oscillator is an extension of the single Lorentz oscillator. According to this theory, the permittivity of a material can be written as follows:

$$\varepsilon(\omega) = \varepsilon_r(\omega) + i\varepsilon_i(\omega) = \varepsilon_\infty\Big(1 - \frac{\omega_p^2}{\omega^2 + i\gamma\omega}\Big) \tag{1.2}$$

where $\gamma = 1/\tau$, τ is the mean relaxation time of conduction electrons, ε_∞ is a contribution due to the interband transition; it is unity for the case of a perfectly free-electron-gas, and ω_p is the plasma frequency. The two main parameters that influence the real and imaginary part of the dielectric function are ω_p and γ.

• ω_p is the plasma frequency. It corresponds to the photon energy position where $\varepsilon_r(\omega)$ is approximately zero. As ω_p increases the amplitude of $\varepsilon_r(\omega)$ and $\varepsilon_i(\omega)$ increases too.

• γ is the collision frequency. As γ increases the broadening of the absorption tail increases too.

The behaviour of the dielectric function:

• $\omega < \omega_p$ then the real part of $\varepsilon(\omega)$ is negative: any electrical field cannot penetrate into the metal. The permittivity of the material is complex.

• $\omega = \omega_p$ then the real part of the dielectric function is close to zero. This means that all electrons oscillate in phase throughout the material propagation length.

• $\omega > \omega_p$ the metal becomes a dielectric and is almost transparent. The refractive index of the material is almost real.

The upper operating frequency boundary for plasmonic systems is thus limited by the plasma frequency of the material that is typically located in the ultraviolet spectrum for noble metals but can be located in the mid-infrared for highly doped semiconductors.

1.1.2 Surface plasmons

At the interface between the dielectric and a metal the coupling between an electromagnetic field with the plasma of electrons leads to a propagating surface wave called *surface plasmon polariton* (SPP). The SPP wave can be easily derived by solving Maxwell's equations at the metal/dielectric interface, assuming a propagation vector along the interface , and evanescent decaying field intensities into both metal and dielectric spaces fig.(1.1). The dispersion relation for the SPP wavevector is well-known and commonly expressed as:

$$k_{SPP} = \frac{\omega}{c}\sqrt{\frac{\varepsilon_m \varepsilon_d}{\varepsilon_m + \varepsilon_d}} \tag{1.3}$$

where ε_m and ε_d are the relative permittivities of the metal and dielectric respectively. The SPP wave exists while ε_m is negative and larger in magnitude than the dielectric permittivity ε_d.

1.1.3 Gap-plasmon wave

When the distance between two metallic plates separated by a dielectric material is small enough to allow the coupling of the two surface plasmon

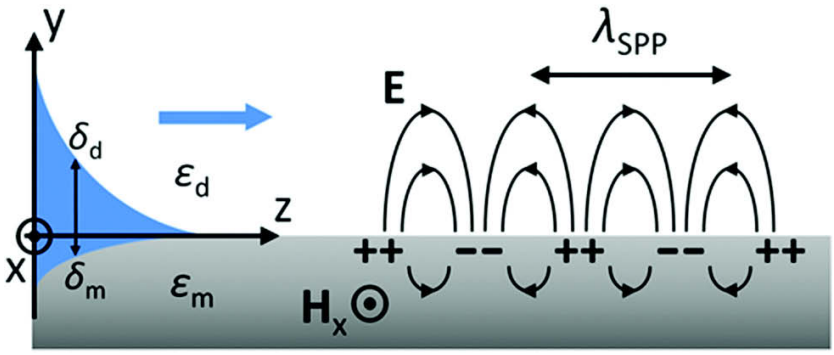

Figure 1.1: Illustration of the field components of a SPP supported by a metal- dielectric interface. The mode is transverse magnetic, exhibiting electric field perpendicular to the interface (y-axis) and along the propagation direction (z-axis). The mode profile (blue) represent the magnitude of the corresponding magnetic field. (reprinted from [3])

waves fig(1.2), a gap plasmon mode is thus generated with an effective index approximated by the following equation:

$$n_{GP} = \sqrt{\varepsilon_d(1 + \frac{2\delta_m}{w})} \tag{1.4}$$

where $\delta_m = c/\omega_p$ is the metal skin depth within the Drude model. It is clear from eq.(1.4) that decreasing the thickness of the dielectric spacer w will increase the effective index of the gap plasmon mode [4, 144, 94].

1.2 Noble metals for plasmonics in the visible

Noble metals such as (Au, Ag, Cu) were admired primarily for their ability to reflect light. Now a days these metals are widely used in electronics and catalysis and as structural materials, but when they are fashioned into structures with nanometer-sized dimensions, they also become enablers for a completely different set of applications that involve light far beyond just reflection. Among metals the significant properties of silver and gold such as the high conductivity and the low loss in the visible and near-infrared (NIR) ranges made them undoubtedly the most used material for plasmonic applications. For example, silver was used for the demonstration of a superlens [5, 6], a hyperlens [7], a negative-refractive-index material in the visible range

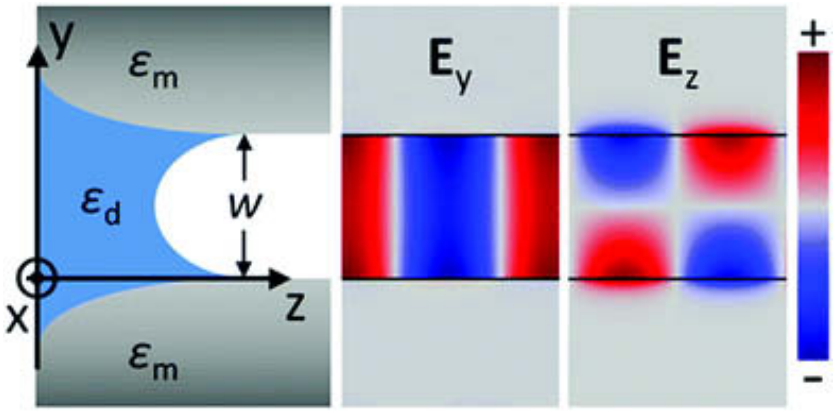

Figure 1.2: Illustration of the field components of a symmetric gap plasmon mode propagating along the z-direction supported by two metal surfaces with a dielectric gap of width w between. With the normal component E_y and the tangential one E_z (reprinted from [3])

[8], and extraordinary optical transmission [9]. Gold also was used in many studies on Surface-Enhanced Raman Scattering (SERS)[51], and for the first demonstration of a negative-refractive index material in the NIR range [10]. Moreover, alkali metals such as sodium and potassium have the lowest losses [64], but these materials are very reactive to air and water and they need to be stored in restricted conditions such as Ultra High Vacuum (UHV) which prohibits their fabrication.

1.3 Searching for better plasmonic materials

As mentioned in the previous sections, plasmonics improves optical systems in the visible range of light. Extending this field to the infrared and THz ranges is essential for variety of technological applications such as imagery, sensing, and security [56]. In particular, many molecules have strong vibrational and rotational absorption lines between $(3 - 30\mu m)$[71]. Also, plasmonic structures might enable the miniaturization of optical structures [11]. Moreover, plasmonic structures that perfectly absorb light at specific wavelength can be considered also as perfect emitters allowing the selective emission of radiation [55]. Despite all the advantages that plasmonics offers, the choice of materials has significant implications for their efficiency. Indeed,

the common plasmonic materials are noble metals like silver or gold which are expensive, not tunable and not CMOS compatible. This prevents their easy fabrication and commercialization. Moreover, in the long wavelength range, because of the huge increase of the absorption losses for noble metals, the coupling of electromagnetic field with the carriers decreases which leads to diminish the plasmonic effects. So the search of alternative plasmonic materials that can overcome those limitations is well desired. Many researches had been done to find materials that can offer efficient plasmonic performances in the visible and the infrared ranges such as, transition metal nitrides, transparent conduction oxides, silicides, doped semi conductors, and graphene. It is worth noting that graphene (i.e one-atom-thick layer of carbon), possesses exceptional electronic properties [12]. The unique band structure of graphene has led to fascinating phenomena, described by massless Dirac fermion physics. The relativistic energy spectrum of the charged particles in graphene leads to the unusual collective behavior of 2D electron or hole gas systems in graphene-based heterostuctures [13, 14, 15, 16].

1.4 Doped semiconductors

Conventionally, semiconductors can be considered as dielectrics for frequencies above several hundred THz. However, in some semiconductors the density of free carriers can be so high that they start to act in a manner similar to noble metals but in the far IR and terahertz (THz) ranges. These conducting materials differ in their electronic band structures, which determine many properties, both electrical and optical. According to Drude Model the plasma frequency ω_p characterizes the collective oscillations of free carriers in the metal which is one of the main properties in a plasmonic structure:

$$\omega_p = \frac{2\pi c}{\lambda_p} = \sqrt{\frac{Ne^2}{\varepsilon_0 m_e}} \tag{1.5}$$

where N, e, ε_0, m_e, are respectively the carrier density, the electron charge, the permittivity of the of free space, and the electron effective mass. For noble metals, the plasma frequency ω_p which is in the deep ultra-violet UV range depends on a constant number of electrons N that cannot be changed, results obtained from Ref [76], Table 1. Additionally, noble metals have limited losses in the visible range since the imaginary part of the electric

permittivity $\varepsilon(\omega)$ is small and sometimes can be neglected. However when moving to the infrared IR and the THz ranges real and imaginary parts of the permittivity are very high and have a considerate effect on the response of the material. Specifically, the imaginary part increases the losses while the real part decreases the plasmonic behaviour. Therefore no plasmonic resonances arise since light cannot penetrate inside the metal which can be considered as a perfect electric conductor (PEC).

	ε_{int}	$\omega_p(eV)$	$\lambda_p(nm)$	$\Gamma(eV)$
silver	3.7	9.2	134.8	0.02
gold	6.9	8.9	139.3	0.07
copper	6.9	8.7	139.3	0.07
Aluminum	0.7	12.7	97.6	0.13

Table 1.1: Drude model parameters for metals

So monitoring the permittivity of semiconductors in the IR and THz is a great advantage. One must understand the intrinsic properties of these materials that allows them to be promising candidates to extend plasmonics to large wavelength ranges (i.e IR and THz). The best-known semiconductor are undoubtedly silicon (Si) and germanium (Ge) which have similar crystalline structure. These elements belong to the group IV in the periodic table. Other semiconductors are compounds formed from elements of the group III and V of the periodic table such as (GaAs, GaSb, InAs...) have properties similar to the group IV counterparts. In going from the group-IV elements to the III-V compounds, the bounding becomes partly ionic due to the transfer of electronic charge from group III to V atoms. The ionization causes a significant change in the semiconductor properties. It increases the Coulombs interaction between the ions and also the energy of fundamental gap in the electronic band structure. The main characteristic of a semiconductor is the ability to modify its conductivity by changing the concentration of the mobile charged carriers (i.e free electrons) according to the equation:

$$\sigma = Ne\varsigma \tag{1.6}$$

where σ is the conductivity and ς is the mobility of the electrons. This modification is called doping where the dopant is integrated into the lattice structure of the semiconductor and the number of outer electrons define the

type of doping. The doping process is categorized in two sections p-doping or n-doping. When the doping element mechanism provides supplementary electrons to the material it is called n-doping, while increasing the number of holes (i.e electron vacancy) is called p-doping.

1.5 Terahertz (THz) technology and applications

Since the last decade, an increased interest is paid to THz ($1 - 100\mu m$) technology, spectroscopy, and imaging for security applications. Some of the

(a)

Material	Feature band centre position frequency (THz)
Explosive	
Semtex-H	0.72, 1.29, 1.73, 1.88, 2.15, 2.45, 2.57
PE4	0.72, 1.29, 1.73, 1.94, 2.21, 2.48, 2.69
RDX/ C4	0.72, 1.26, 1.73
PETN[a]	1.73, 2.51
PETN[b]	2.01
HMX[a]	1.58, 1.91, 2.21, 2.57
HMX[b]	1.84
TNT[a]	1.44, 1.91
TNT[b]	1.7
TNT	5.6, 8.2, 9.1, 9.9
NH_4NO_3	4, 7
Drugs	
Methamphetamine	1.2, 1.7–1.8
MDMA	1.4, 1.8
Lactose α-monohydrate	0.54, 1.20, 1.38, 1.82, 2.54, 2.87, 3.29
Icing sugar	1.44, 1.61, 1.82, 2.24, 2.57, 2.84, 3.44
Co-codamol	1.85, 2.09, 2.93
Aspirin, soluble	1.38, 3.26
Aspirin, caplets	1.4, 2.24
Acetaminophen	6.5
Terfenadine	3.2
Naproxen sodium	5.2, 6.5

(b)

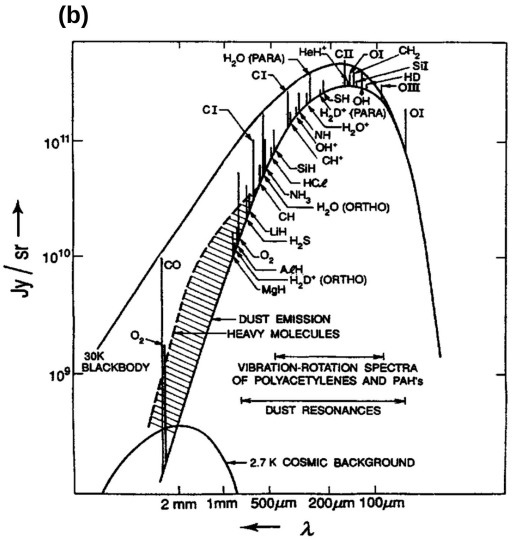

Figure 1.3: (a) Collection of absorption peak positions of some explosives and drugs(reprinted from [56]). (b) Radiated energy versus wavelength showing 30-K Black body, typical interstellar dust, and key molecular light emissions in the submillimeter (reprinted from [26])

main motivations to explore deeply this spectral region is that THz radiation can detect concealed weapons, target compounds such as explosives, and drugs that have characteristic THz spectra, that can be used as a fingerprint for these materials and compounds fig.1.3(a) [56]. In addition to its beneficial applications, THz radiations poses no health risks to humans. Also

astronomers shows a big interest in terahertz sensor technology. Fig. 1.3(b), shows the radiated energy with respect to the wavelength for interstellar dust, heavy molecules, and a 30-K black body radiation curve. Noting that the interstellar dust clouds emits 40000 spectral lines, only few thousands had been identified. Results from the NASA Cosmic Background Explorer (COBE) Diffuse Infrared Back ground Experiment (DIRBE) and the examination of the spectral energy distributions in observable galaxies, indicated that approximately one half of the total luminosity and 98% of the photons emitted since the Big Bang fall into the submillimeter and far-infrared, making THz detectors true probes into the early universe. From security and astronomy, THz technology benefits expand to biology and medicine. This can serve a lot of applications spanning from detection and tumor recognition to disease diagnostics[17], recognition of protein structural states [18], monitoring of receptor binding [19], performing label-free DNA sequencing [20], visualizing and cataloging absorption and contrast mechanisms in otherwise uniform tissue [21], and radiation effects on biological samples and biological processes [22, 23].

1.6 MIM resonators

One of the promising geometries of plasmonic structures that can well serve the improvement of the terahertz technology are metal-insulator-metal (MIM) antennas. They had prove to posses many fascinating properties due to their simple design and predictable physical mechanisms that allows the concentration of the electromagnetic fields inside the insulator layer. In these antennas the strong localization of plasmonic modes increases light-matter interactions allowing the realization plasmonic waveguides for laser emission, switchable devices and tunable perfect absorbers [24, 25, 50]. They also have demonstrated to boost the Purcell factor by placing fluorescent molecules near the intensified field which allow them to emit photons of light 1000 times faster than the conventional designs fig1.4(left). This enhancement in the Purcell factor is a step toward realizing super-fast light emitting diodes (LEDs) for photonic devices, such as telecomunication lasers and as single-photon sources for quantum cryptography [49]. Solar energy harvesting is also a very simple way to benefit from these geometries. One of these approaches is to sprinkle silver nanocubes over a polymer coated gold, the result is a drastic increase in the absorption of the system this promising technique

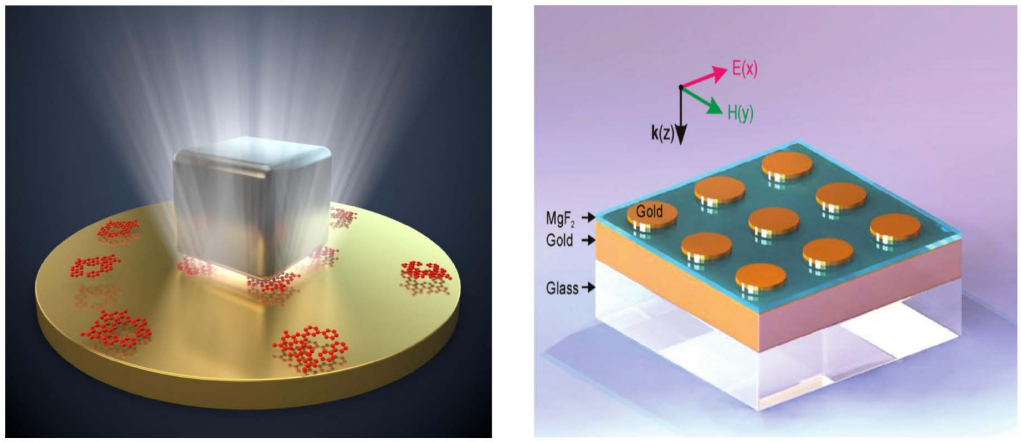

Figure 1.4: (Left) 3D illustration of the nanocubes surrounded by florescent molecules, (right) Schematic representation of Gold-MgF_2-Gold resonators for glucose sensing reprinted from [84].

had firstly been experimentally realized in 2012 [96]. Sensing technology is also a branch that can use the plasmonic resonances in a MIM resonator to identify chemical solutions such as glucose fig.1.4(right) [84]. All these applications proves that these simple and flexible geometries can provide a very significant impact on the development of many technologies.

1.7 Metamaterials

Materials found in nature owe their properties (i.e permittivity ε, and permeability μ) from the atoms and molecules that they are composed of. On the other hand, in metamaterials atoms and molecules are replaced by man made structures that might have dimensions of nanometers for visible light and to few millimeters in the case of GHz radiations. We can say that metamaterials gain their properties from their geometrical structure (i.e ε_{eff}, μ_{eff}), while natural materials through their chemical compositions fig(1.5). Metamaterials fascinate scientists because of their varied applications including imaging [27, 28], cloaking [29], sensing [30], waveguiding [31], and simulating space time phenomena [32].

A well known optical property for metamaterials is the possibility to realize a negative refractive index. Since the size of the geometrical manufac-

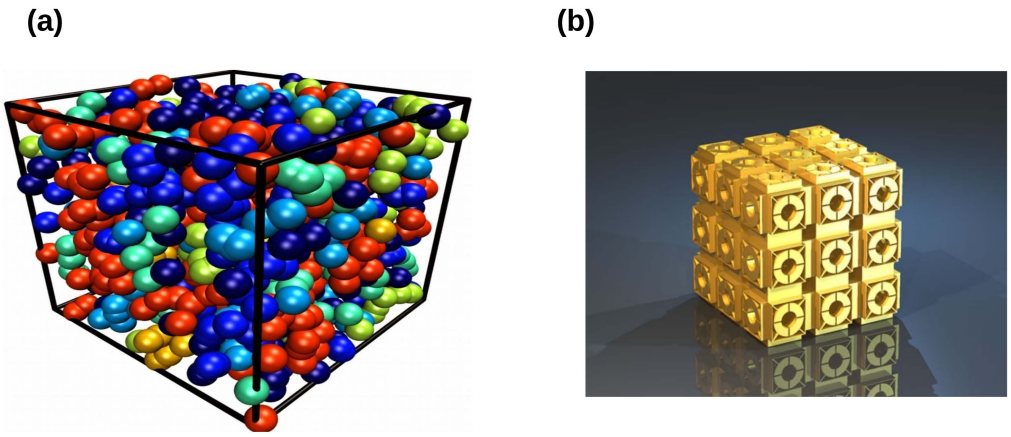

Figure 1.5: (a) Illustration of conventional materials made up of atoms, ε and μ are derived from the constituent atom. (b) A model of 3-D metamaterial where ε_{eff} and μ_{eff} are derived from the geometrical sub-units.

tured unit cells are much smaller than the wavelength, the over all structure presents an effective permittivity and an effective permeability (ε_{eff}, μ_{eff}). When these ε_{eff} and μ_{eff} are both negative one can define a negative effective index:

$$n_{eff} = -\sqrt{\mu_{eff}\varepsilon_{eff}} \tag{1.7}$$

This negative sign introduced in the index implies that the flow of energy

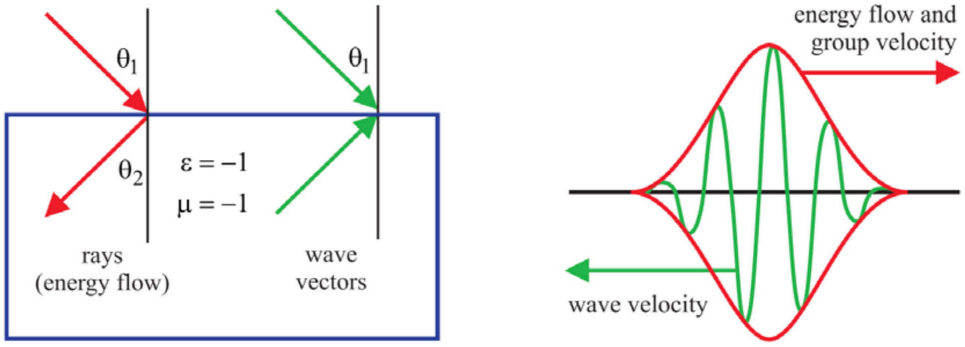

Figure 1.6: (a) Illustration of the energy flow vectors and the wave vectors in in a negative index material. (b) The wave velocity and the group velocity travel in the medium in opposite directions.

and the phase velocity propagate in opposite directions fig.(1.6). In that case the metamaterials are also named "Left-handed" materials. Negative index materials were first demonstrated experimentally at microwave frequencies using split ring resonators fig.(1.7.a) [37, 38]. These results encouraged researchers to design metamaterials that function at higher frequencies (i.e visible range), this require unit cells of 100 nm or even smaller. A simpler way is adopted by the group of Xiang Zhang where the negative refraction is obtained by stacking 11 functional layers of fishnet structures that operates at near infrared wavelengths fig.(1.7(b)).

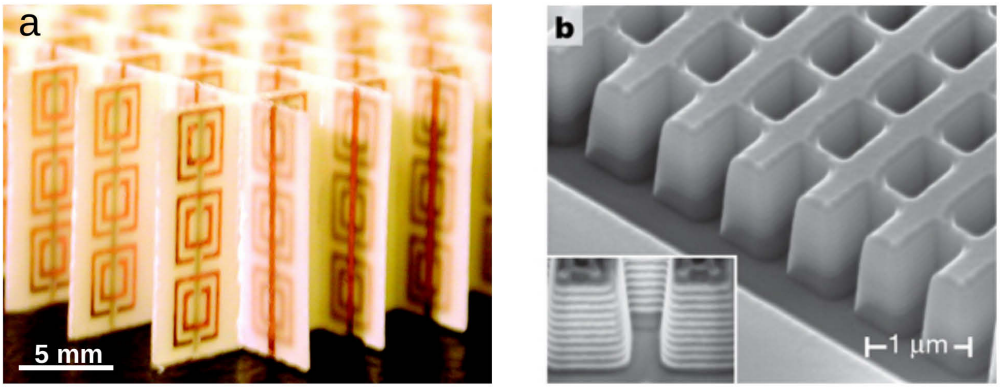

Figure 1.7: (a) A photograph of a negative index metamaterial function in the microwave range, it consists of square copper split ring resonators and copper wire strips on a fibre glass circuit board material. (b) SEM image of a fishnet structure function at visible frequencies, the structure consist of alternating layers of 30 nm silver (Ag) and 50 nm magnesium fluoride (MgF_2). (a) and (b) are reprinted respectively from [38, 39]

Negative index materials have also been realized and experimentally demonstrated in the near infrared range [33, 34]. Other recent results show that metamaterials can also exhibit a near-zero refractive index in the visible and infrared ranges, which is very promising in the fields of cloaking, super reflection and tunneling [35].

One class of highly anisotropic metamaterials called hyperbolic metamaterials (HMMs) has recently attracted lot of attention. Their name is derived from the topology of the isofrequency surface. For isotropic materials the optical dispersion is defined by spherical isofrequency surfaces (fig.1.8a) given

by the following equation:

$$k_x^2 + k_y^2 + k_z^2 = \frac{\omega^2}{c^2} \tag{1.8}$$

where k_x, k_y, k_z are respectively the x, y, and z components of the wavevector, ω is the wave frequency, and c is the speed of light. While in the hyperbolic metamaterials the effective permittivity and permeability are presented as tensors, where one of their components is opposite in sign to the other two:

$$\varepsilon = \begin{pmatrix} \varepsilon_{xx} & 0 & 0 \\ 0 & \varepsilon_{yy} & 0 \\ 0 & 0 & \varepsilon_{zz} \end{pmatrix}, \mu = \begin{pmatrix} \mu_{xx} & 0 & 0 \\ 0 & \mu_{yy} & 0 \\ 0 & 0 & \mu_{zz} \end{pmatrix}, \tag{1.9}$$

In the two-dimensional case and for TM polarized waves, the dispersion relation is given by:

$$\frac{k_x^2 + k_y^2}{\varepsilon_{zz}} + \frac{k_z^2}{\varepsilon_{xx}} = \frac{\omega^2}{c^2} \tag{1.10}$$

This relation appears as open hyperboloid isofrequency surfaces as shown in fig.(1.8(b,c)). These materials can behave like a metal in one direction and dielectric in the other. These materials are classified into two types: Type I HMMs acts as a dielectric material in the x-y directions (ε_{xx}=ε_{yy}=$\varepsilon_{\perp} > 0$), and metallic in the z-direction (ε_{zz}=$\varepsilon_{\parallel} < 0$). While type II have its metallic behaviour in the x-y directions ($\varepsilon_{xx} = \varepsilon_{yy} < 0$), and the dielectric in the z-direction ($\varepsilon_{zz} > 0$).

Hyperbolic metamaterials can be realized either in one dimension or in two. One dimension structures (1-D) are formed from alternating layers of metal and dielectric fig.(1.9 a). The two dimensional (2-D) HMMs are made of a periodic set of metallic nanowire fig.(1.9 b). Due to the simple 1D geometry and to their unusual optical properties, hyperbolic media have become very important and are predicted to find widespread applicability in many applications.

1.8 Merging of plasmonics and metmaterials

As described previously, the natural electromagnetic spectrum where plasmonics is studied is the visible range and many efforts are made to extend it to the infrared and microwave regimes. On the other hand, metamaterials were original demonstrated in the microwave region. But plasmonic

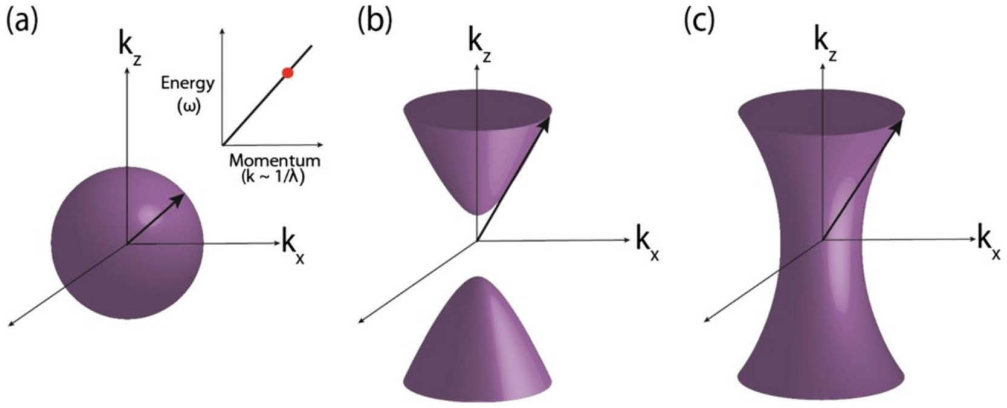

Figure 1.8: (a) Spherical isofrequency surface for isotropic dielectric. (b and c) Are respectively the isofrequency surfaces of (Type I HMM: $\varepsilon_{zz} < 0; \varepsilon_{xx} = \varepsilon_{yy} > 0$), and (Type II HMM: $\varepsilon_{zz} > 0; \varepsilon_{xx} = \varepsilon_{yy} < 0$). reprinted from [36]

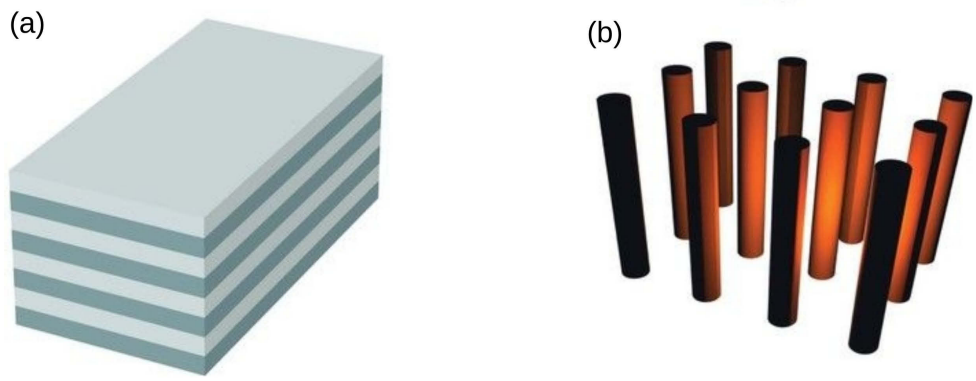

Figure 1.9: (a) Multilayer structure consisting of alternating metallic and dielectric layers. (b) Nanowire structures consisting of metallic nanorods embedded in a dielectric matrix.

resonances appear when one try to shift the electromagnetic properties of metal based metamaterials in the visible range. Consequently plasmonics and metamaterials merge in the visible and infrared ranges leading to generate a lot of new concepts and approaches. For example the dispersion of the surface plasmon polaritons SPPs can be used to get Left-handed properties as demonstrated in Ref. [40, 41]. These properties were utilized in an array of metal-dielectric-metal waveguides that theoretically present a 3-D

negative refractive index at the visible frequencies [42].

Because of the technological challenge imposed by the metamaterial fabrication, simple 2D structures named metasurfaces were developed. These 2-D surfaces are realized by patterning plasmonic nanostructures and distribute them along a dielectric layer. These structures can achieve various optical phenomena ranging from negative refraction, to ultra thin focusing and diverging lenses. This approach allows to manage the local phase response by considering a two dimensional gradual array of optical resonators fig.(1.10.a) [43]. Moreover, a theoretical and experimental demonstration of a gradient index metasurface can convert a propagating wave into a surface wave which can be useful in anti-reflection, invisibility, and light absorption applications fig.(1.10.b) [44].

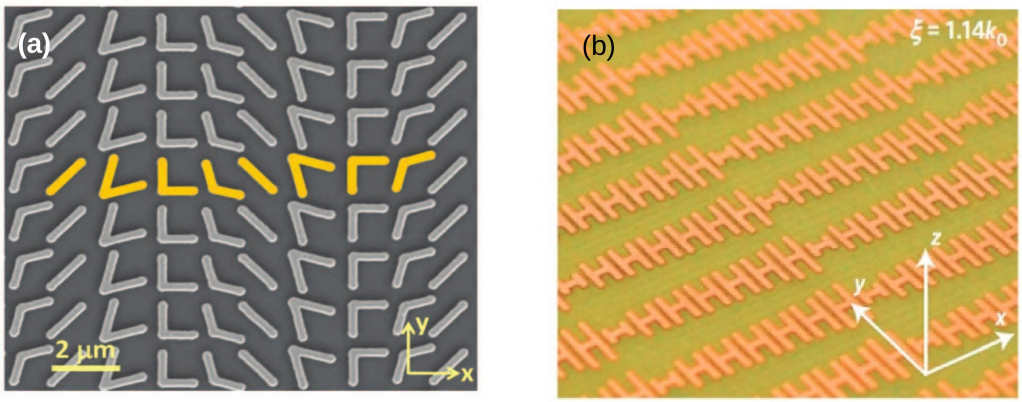

Figure 1.10: (a) SEM image of antenna array fabricated on silicon wafer, the yellow antennas are gold v-antennas, reprinted from [43], (b) Photograph of a fabricated microwave reflect-array consisting of H-antennas separated from a metallic back plane by a dielectric spacer, reprinted from [44]

1.9 Conclusion

As described previously, the development of THz technologies needs to extend the plasmonic properties to this range of frequency. How can we make this? In this thesis, we address this issue by using highly doped semiconductors in order to substitute noble metals. To validate this approach, we theoretically and experimentally study MIM antennas made of highly doped semiconduc-

tor. Next, we combine the MIM geometry with the exotic response of hyperbolic metamaterials to overcome the MIM antennas limitations. Finally, the extreme choice of geometrical parameters of a grating metamaterial absorber, allow us to reach perfect absorption and overcomes the material barrier that usually imposes the spectral range of the electromagnetic response.

Chapter 2

MIM antennas in the far-infrared range

In the last decades plasmonic systems have known an increasing interest owing to their ability to enhance and confine free-space electromagnetic waves into subwavelength regions. Among the various plasmonic geometries studied such as the bow-tie, the v-antenna, and the stacked optical antenna [45, 46, 47, 48], Metal-Insulator-Metal (MIM) resonators are particularly attractive. They have been demonstrated to boost the Purcell factor and the light extraction, or to behave as perfect and tunable absorbers [50, 49]. The majority of plasmonic resonators including MIM antennas are utilized in the visible to near-infrared (400-2000 nm) where several applications domains such as biosensing, or photovoltaics benefit on the plasmonic effects [51, 52, 53, 54]. Extending the use of plasmonics in the far-IR and terahertz (THz) ranges becomes crucial for the next communication, imaging and sensing, security and biomedical applications [56, 57, 58, 59, 55]. However, the development of plasmonic systems operating in the far-IR and THz is still facing challenges concerning metal choice and fabrication.

2.1 Noble metals are not the perfect candidate for MIM antennas in the THz

In THz range, the absolute value of the permittivity of the noble metals is very large forbiding the light to penetrate in the metal. For this reason the plasmonic effects are extremely limited. That will impact drastically the de-

sign of the plasmonic resonator fig.(2.1.b). In addition, the strong dispersion of the optical properties (refractive index and absorption coefficient) of Drude metals prevents applying simple scaling laws for transposing any plasmonic architectures from the visible to the THz ranges [60]. Also, the losses caused by the free carriers dominate due to the inter-band transitions in noble metals, which in turn degrades the optical efficiency of plasmonic systems in the far-IR. All these constrains explain why it is challenging to shift plasmonic resonances of MIM antennas beyond the near-IR range [55, 60, 61, 147, 62] except in some extreme geometrical conditions [90]. Finally, gold is not compatible with the CMOS technology and silver oxidise in the THZ rang which prevents their straightforward integration.

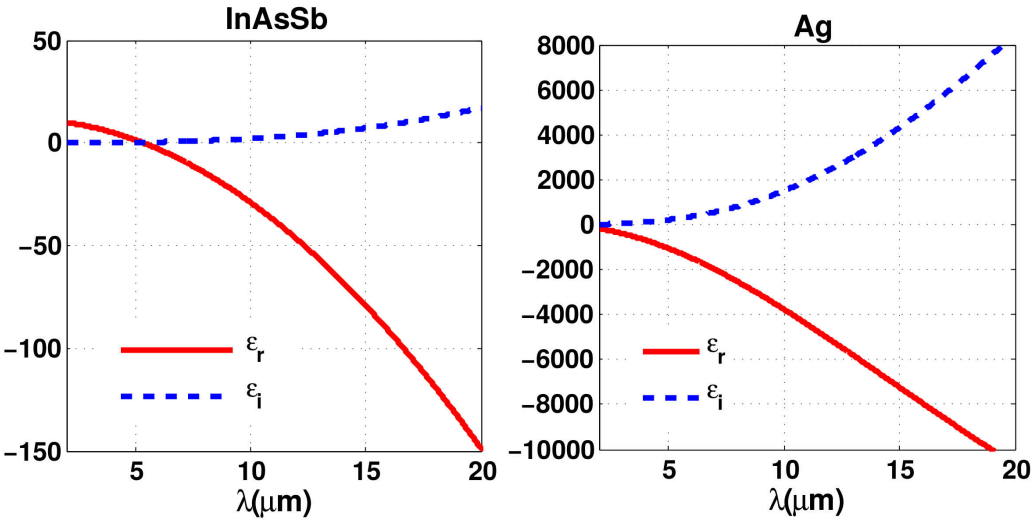

Figure 2.1: (a) and (b) represent respectively the real and imaginary part of the electric permittivity of HDSC InAsSb and silver (Ag).

So to overcome the limitations due to materials barriers, new materials presenting a metallic behavior from far-IR to THz ranges are thus needed. A study of inter-metallic compounds to find the ideal plasmonic material had been made to reduce the losses, but the degree of controlling losses is still a constraint [63]. Alkali metals are also a good candidate for low-loss plasmonic structures, but they are very reactive to air and water which make them dangerous substances and therefore prohibit their fabrication [64]. Therefore, using highly doped semiconductors (HDSC) is an elegant approach

to realize metallic-like materials at the desired range of frequency since the plasma frequency, which depends on the electronic density, can be adjusted by monitoring the doping level [66, 65]. In addition to their easy tunability, HDSC are compatible with CMOS technology making them good candidates for future commercial applications. Recent works have highlighted different kinds of HDSC plasmonic behaviours in the infrared ranges based in doped silicon [67], GaAs [68], germanium [69], and InAs [70, 71, 119].

In this chapter,we report the first experimental demonstration of plasmonic MIM antennas made of HDSC and operating in the far-IR. The HDSC InAsSb will be Si doped lattice matched on GaSb substrate. This HDSC combined with a dielectric GaSb allow to design the MIM resonators in the THz range. The MIM structures consist of a dielectric spacer sandwiched between a metallic upper part which is periodically textured, and a back mirror. In these structures demonstrate a near perfect absorption resulting from the combination of the gap plasmon and a Fabry-Perot resonance mode[4].

2.2 Silicon doped InAsSb

In this work a highly Si-doped InAsSb is used, where the Si atoms are considered as an amphoteric element (i.e the role of Si depend on the element it replace). Si can act as a p-doping if it replace a group V elenent or n-doping if it takes the place of some In atoms (i.e group III element). This mechanism provides supplementary electrons to our material (i.e n-doping) which gives InAsSb the metallic character for plasmonics in the IR.

The highly doped semiconductor InAsSb alloys are used because of their specific physical properties. First, $InAs_{0.91}Sb_{0.09}$ (91% As and 9% Sb) is lattice matched to GaSb substrate guaranteeing the high crystalline quality of the samples. Second $InAs_{0.91}Sb_{0.09}$ is one of the easiest material to dope[77]. Third, the small effective mass of InAsSb alloys [79] allows reaching a high plasma frequency. Finally, the conduction band offset between InAsSb and GaSb avoids charge transfer from the metal-like InAsSb into the substrate [65, 78].

2.3 Design and theory of the MIM antennas

As mentioned before the common geometry of MIM resonators is a dielectric layer between two metallic plates. In a MIM geometry it is needed to limit the size of one of the two metallic plates to make a pitch, this condition allow the coupling of the far field, while the second metallic plate acts as a mirror to prevent any transmission so the light can be trapped in the spacer. It has been well established that MIM cavities produces strong resonance modes resulting from the standing-wave of the surface plasmons in the gap. Decreasing the gap size of the cavity can lead to extremely large field enhancements in the spacing layer.

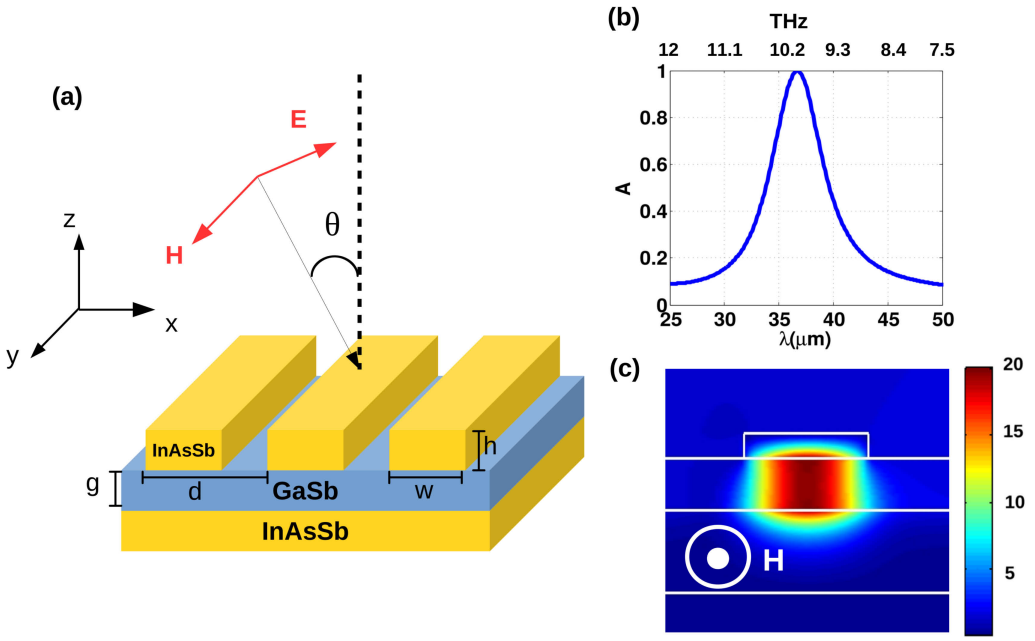

Figure 2.2: (a) Representation of the antennas with w and g are the width of the antenna and the thickness of the dielectric respectively. (b) Spectrum of the absorption coefficient of the antennas with $w = 3\mu m$, $h = 300nm$, $g = 630nm$, and $d = 10\mu m$, (c) Magnetic field profile of the gap plasmon mode located under the antenna.

The MIM antennas proposed are formed of a dielectric spacer GaSb sandwiched between a back mirror and a periodic set of InAsSb:Si strips fig.2.2(a). The thickness of the spacer GaSb is denoted by g with permittivity $\varepsilon_d = 13.4$

assumed to be constant [72]. The InAsSb material is the HDSC whose relative permittivity can be described by an adapted expression of the Drude model:

$$\varepsilon_{InAsSb} = \varepsilon_\infty \Big(1 - \frac{\omega_p^2}{\omega(\omega + i\gamma)}\Big) \tag{2.1}$$

where $\varepsilon_\infty = 10.4$, $\gamma = 10^{13}\, rad.s^{-1}$, and the plasma frequency $\omega_p = 351.10^{12}\, rad.s^{-1}$. We determined $\omega_p = 351.10^{12}\, rad.s^{-1}$ experimentally by measuring the Brewster mode [118]. The period is considered to be larger than the antenna width, in order to consider that the MIM resonator are electromagnetically uncoupled. In this framework, the incident electromagnetic wave with a magnetic field polarized along the antenna array couples into a plasmonic mode (i.e gap plasmon), guided inside the dielectric spacer, fig.2.2(c).

2.3.1 Effective index method (EIM) of the gap plasmon

The first doorway to understand the physics of the MIM antennas is by deriving the expression of the effective index of the gap plasmon mode. This plasmonic mode is a coupling between two surface plasmon polaritons SPP at the two interfaces of the metal dielectric slabs. This coupling allows the trapping of the wave between two metallic planes separated by a dielectric spacer of subwavelength thickness. So in order to obtain the expression of the effective index n_{gap} of the gap plasmon mode one can derive the expression for gap plasmon propagation constant.Applying the appropriate boundary conditions for the magnetic field components allows to obtain a relation between the propagation constants inside the metal and the dielectric:

$$tanh(\frac{k_z^d g}{2}) = -\frac{\varepsilon_d}{\varepsilon_m}\frac{k_z^m}{k_z^d} \tag{2.2}$$

with

$$k_z^{(m,d)} = \sqrt{k_{gap}^2 - \varepsilon_{m,d} k_0^2}, \qquad k_0 = 2\pi/\lambda_0 \tag{2.3}$$

Where g is the gap thickness, ε_m and ε_d are the electric permittivity of the metal and dielectric respectively, and k_{gap} denotes the propagation constant of the fundamental gap propagation constant.Solving equations (2.2) and

(2.3), an expression of the effective index can be obtained:

$$n_{gap} = \frac{k_{gap}}{k_0} = \sqrt{\varepsilon_d}\left(1 + \frac{\lambda}{\pi g\sqrt{-\varepsilon_m}}\sqrt{1 + \frac{\varepsilon_d}{-\varepsilon_m}}\right)^{1/2} \tag{2.4}$$

Considering the approximation $\mid \varepsilon_m \mid >> \varepsilon_d$, and using the Drude model for the metal permittivity allows to write a very compact expression for n_{gap} eq.2.4:

$$\boxed{n_{gap} = \sqrt{\varepsilon_d\left(1 + \frac{2\delta}{g}\right)}} \tag{2.5}$$

where $\delta = c/\omega_p$ is the metal skin depth within the Drude model. It is obvious that from eq.(2.5) the effective index of the gap plasmon mode is strongly dependent on the thickness of the gap g. So when the thickness of the spacer is reduced to only hundredths of the wavelength the gap-plasmon is slowed down meanwhile its effective index increases [144, 94].

2.3.2 Fabry Perot conditions

It is possible to reach perfect absorption because the Fabry-Perot resonance in the MIM antennas behaves as a cavity for the gap plasmon [4]. So in order to predict the resonant wavelength, we use an approximate Fabry-Perot model which allows us to derive a semi analytical expression to the resonant mode. Within the Fabry-Perot picture, the resonance is described as a standing wave pattern along the z-direction created by the bouncing of the magnetic field in the dielectric medium located under the metallic antenna. According to the phase matching conditions, The resonant wavelength is directly linked to the width of the resonators and the effective index of the gap plasmon mode as following [137]:

$$\lambda_r = 2n_{gap}w + \lambda_\phi \tag{2.6}$$

Where λ_ϕ is a correction phase term. According to eq.(2.6), we can tune the desired wavelength λ_r by changing the two main parameters which are the thickness of the gap g and the width of the rod w. For example, we observe an absorption peak at $\lambda_r = 37\mu m$ at normal incidence for a transverse magnetic wave for antennas of width $w = 3\mu m$ and a height of $h = 0.3\mu m$ on a spacer of thickness $g = 0.63\mu m$, $d = 10\mu m$, Fig.2.2(b). The absorption coefficient A is calculated applying the following equation $A = 1 - R - T$ where the

reflection R and the transmission T are calculated using home-made code based on the rigorous coupled-wave analysis method (RCWA) [80]. This resonant wavelength can be predicted easily by calculating the effective index ($n_{eff} = 4.9$) of the mode and replacing it in equation (2.6) with a correction phase term. It is worth noting that the angle of incidence doesn't affect the gap plasmon mode fig.2.3.

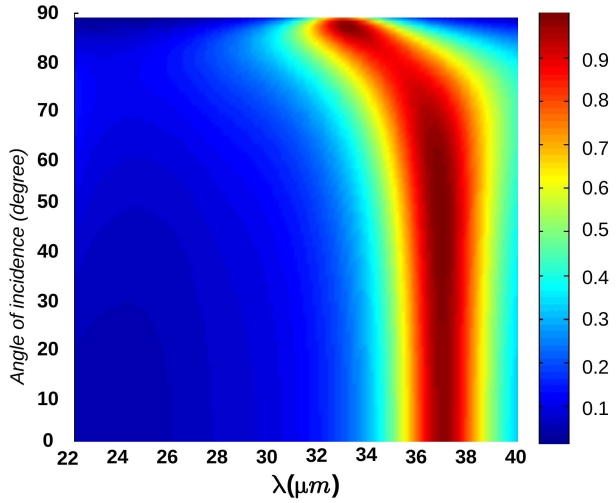

Figure 2.3: (a) Representation of the absorption spectrum as a function of the wavelength and the angle of incidence for $w = 3\mu m$, $g = 0.63\mu m$, $h = 0.3\mu m$ and $d = 10\mu m$.

2.3.3 Theoretical discussion

To go deeper in the analysis of the MIM antennas' behaviour, the increase in the width w will cause a red shift in the resonance that is because the width of the F.P cavity increases and will therefore support a resonance of longer wavelength. This linear behaviour predicted by the equation (2.6) is represented in figure 2.4(a). This map represents the absorption of a structure for $g = 0.63\mu m$ and varying the width of the antennas. Similarly, as the gap narrows, the effective index of the gap plasmon mode increases, which effectively lengthens the cavity, resulting in a resonance condition at a longer wavelength fig.2.4(b). On the other hand the capacity of the dielectric gap to absorb light at very thin thickness is deteriorated so we can observe

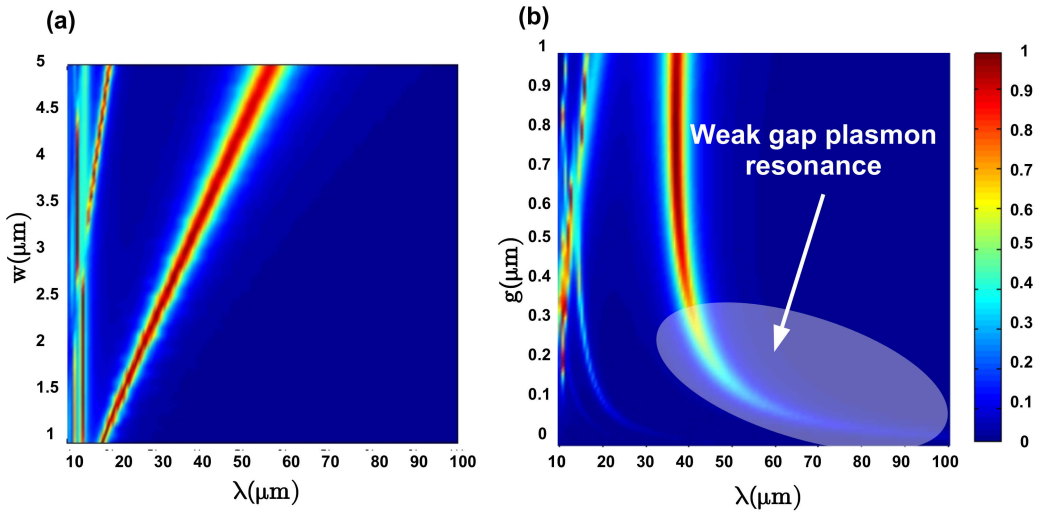

Figure 2.4: (a) Representation of the absorption spectrum as a function of the wavelength and the width of the antenna for $g = 0.63\mu m$, $h = 0.3\mu m$ and $d = 10\mu m$. While (b) is absorption spectrum with respect to the thickness of the gap of antennas of width $w = 3\mu m$, $d = 10\mu m$, and $h = 0.3\mu m$.

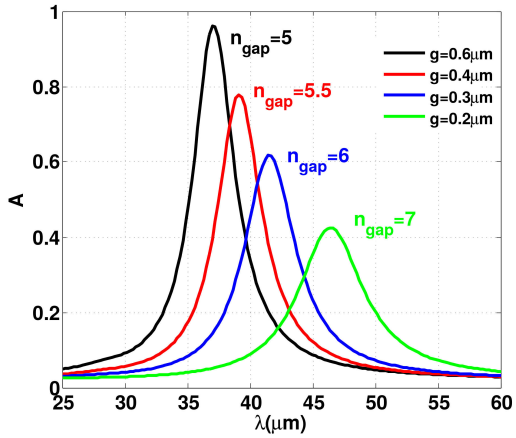

Figure 2.5: The absorption spectra of four MIM antennas of $d = 10\mu m$ and $w = 3\mu m$, where the thickness of the gap g is $\{0.6, 0.4, 0.3, 0.2\}\mu m$ respectively.

clearly that the absorption decrease drastically for thin gaps fig.(2.5). This limitation will be discussed and solved in the next chapter.

2.4 Experimental procedure

To demonstrate experimentally the efficient absorption through the gap plasmon coupling with THz wave, we fabricate an all semiconductor gap plasmon resonators. These MIM resonator structures are subjected to two different steps of realization. First, the layers of InAsSb:Si and GaSb were grown using solid source molecular beam epitaxy (MBE). Second they are fabricated by laser lithography and wet chemical etching. After that, the spectral characterization of the MIM antennas is done using Fourier Transform Infrared (FTIR) spectrometer to measure the reflectance (fig.2.6).

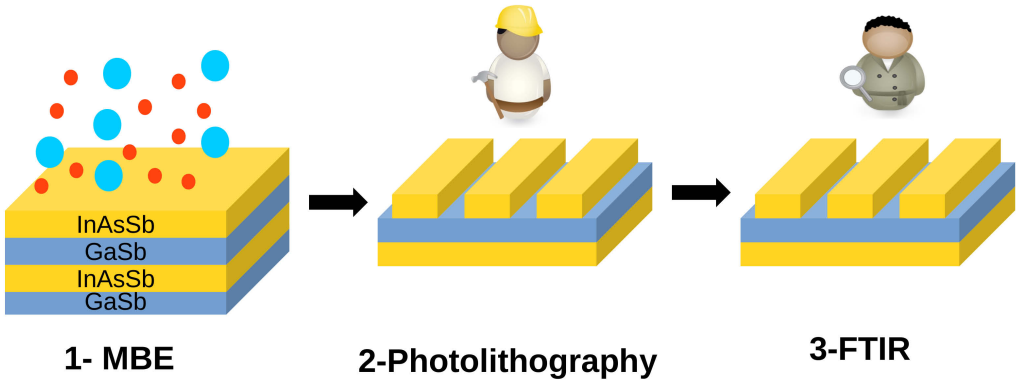

Figure 2.6: Summary of the fabrication procedure of realizing 1- MBE, 2- photolithography , 3- characterization of the MIM resonators by FTIR measurements.

2.4.1 Molecular Beam Epitaxy (MBE) and doping characterization

MBE is a versatile and precise technique for growing thin and multilayer structures such as semiconductors, metals or insulators. It allow to deposit atomic layer after atomic layer giving an ultimate control of the growth. Unlike other epitaxial growth techniques, such as liquid phase epitaxy or vapour phase epitaxy which are proceeded near thermodynamic equilibrium. They are most frequently controlled by diffusion processes occurring in the crystallizing phase surrounding the substrate crystal. MBE is carried out in vacuum under conditions far from the thermodynamic equilibrium. The

deposition process is governed mainly by the kinetics of the surface processes. The impinging beams react with the outer most atomic layers of the substrate crystal. The thin films crystallize via reactions between the thermal-energy of molecular or atomic beams of the constituent elements and the substrate surface which is maintained at an elevated temperature in ultra high vacuum. The composition of the grown epilayer and its doping level depend on the evaporation rates of the appropriate sources. Changes in composition and doping can thus be abrupt at an atomic scale. Consequently, the surface of the grown film can be very smooth.

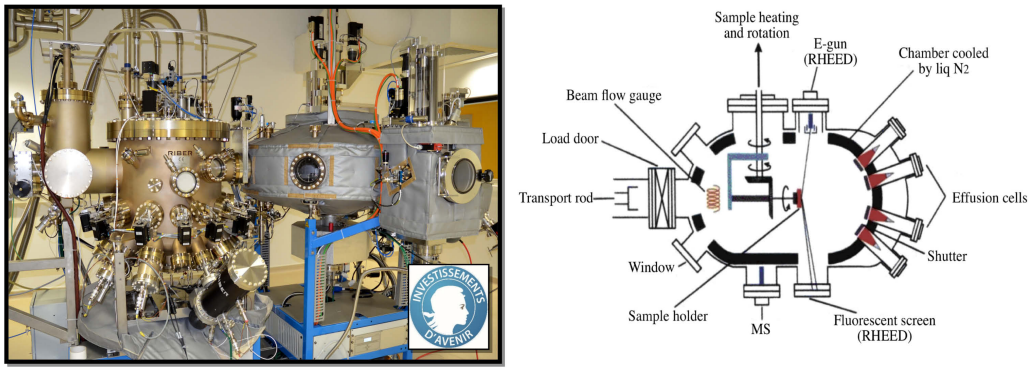

Figure 2.7: (a) photograph of the molecular beam epitaxy machine, (b) schematic diagram of molecular beam epitaxy growth chamber.

In our case, the MIM resonators are grown by solid source molecular beam epitaxy (RIBER, compac 21 growth chamber) as shown in fig.(2.7). The growth procedure is an oxide desorption of the Te-doped (100)-GaSb substrate, followed by the deposit of a mirror of 993 nm of Si doped $InAs_{0.9}Sb_{0.1}$ with a carrier concentration of $5 \times 10^{19} cm^{-3}$, that allows to reach a metallic behaviour for frequency lower than 54 THz. The spacer of 630 nm thickness is a non-intentional doped (nid) GaSb. Finally, a 298 nm thick layer of highly doped n-$InAs_{0.9}Sb_{0.1}$ of the same doping level is grown. The high resolution X-ray diffraction was measured showing a compressive lattice mismatch inferior to 0.07% as shown in fig.2.8(d).

The angular-dependent reflectance measurements of plain InAsSb layers lattice matched onto GaSb substrate fig.2.8(a), shows a dip in the reflection spectrum at 0.182 μm^{-1} (5.1 μm).This dip obtained in p-polarized light corresponds to the Brewster mode fig.2.8(c) [118]. This peak of absorption is due to the free carriers of the layer. Monitoring the doping level modifies the

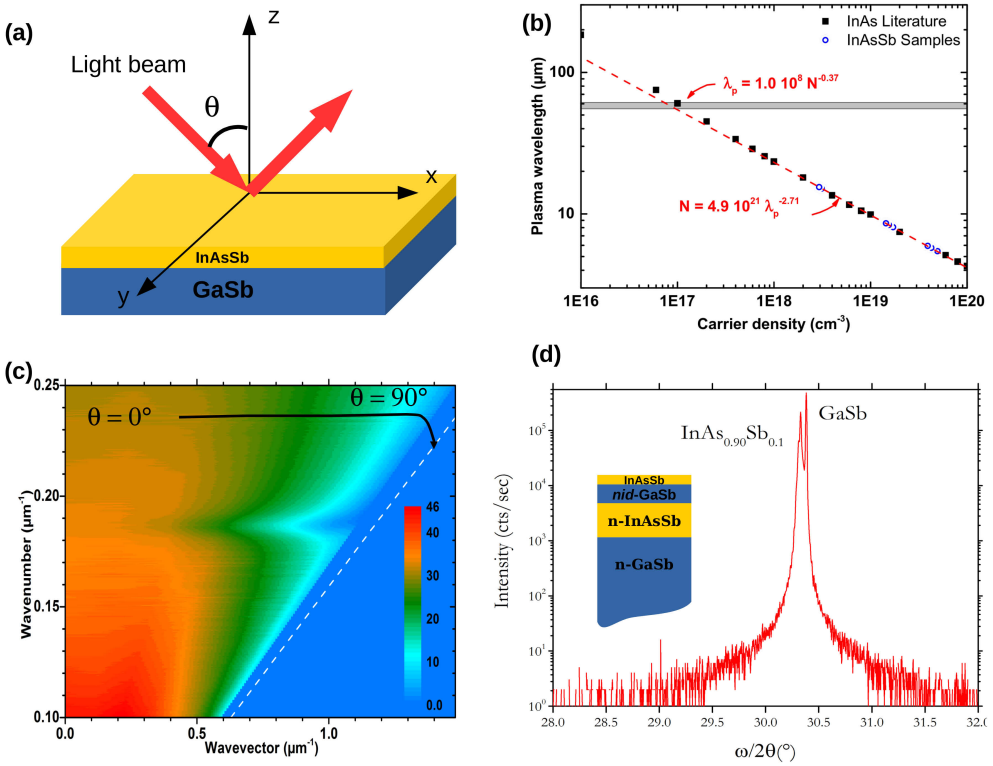

Figure 2.8: (a) Diagram for the incoming and the outgoing light beam, (b)plasma wavelength, versus the carrier density in the case of InAsSb, the red dashed line correspond to the power law extracted from experiment, while the black and blue dots correspond to the experimental values of InAs and InAsSb respectively, (c) Reflectance dispersion under TM polarization of a 100 nm InAs layer obtained by angular resolved reflectance experiment. The dashed line is the light line in air. (d) X-ray diffraction data showing the mismatch between the InAsSb and GaSb layer.

plasma frequency and reduces the negative value of the permittivity in the range of application. In the case of thin layers, the Brewster mode is close to the plasma wavelength λ_p, which is proportional to the carrier density eq.(1.5). It is noticeable that the spectral position of the Brewster mode can be used to accurately measure the doping level of the doped semiconductor during the epitaxial growth. Figure 2.8(b) shows the variation of λ_p as a function of the carrier density in the case of InAs [81]. The red and the

square lines are the theoretical and experimental values respectively[118].

2.4.2 Resonator fabrication: Laser lithography and wet chemical etching

After the growth procedure of the layers, the next fabrication step is laser lithography which is the process of transferring geometric shapes of a mask to a surface.

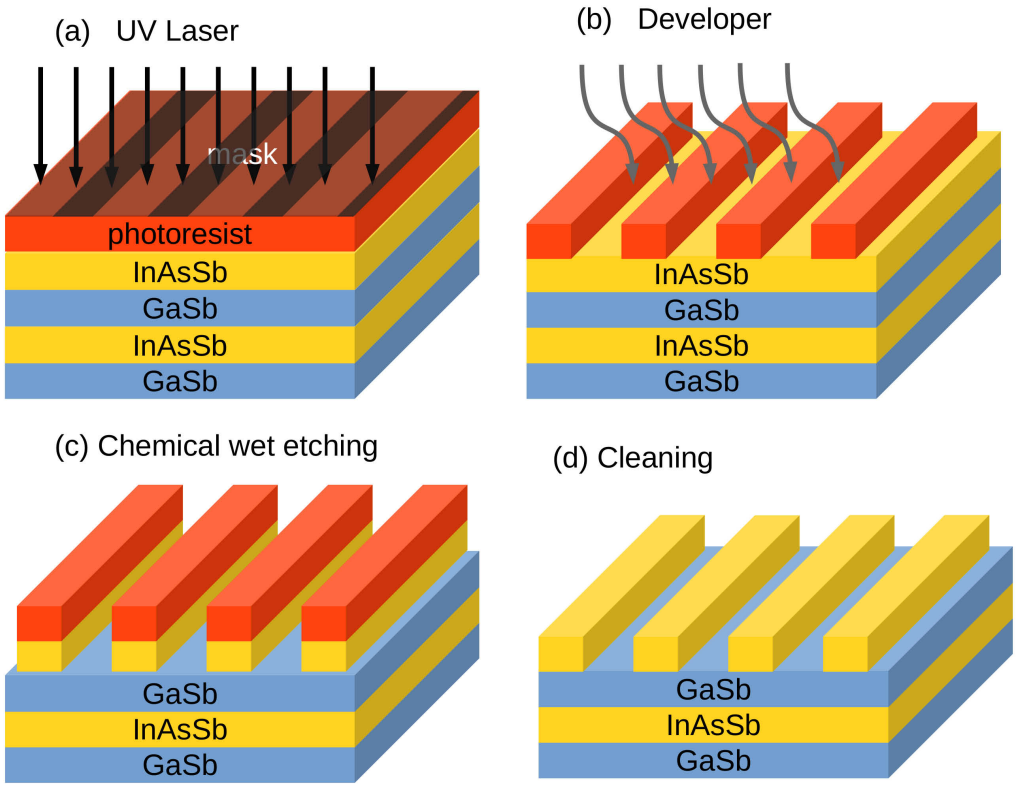

Figure 2.9: Technological process of the MIM resonators. (a) placing the positive photoresist and then the UV photolithography, (b) resist development, (c) chemical wet etching by using a solution $C_6H_8O_7 : H_2O_2$ with a 2:1 ratio. The width of the resonators is controlled by the etching time. (d) Photoresist removal and surface cleaning of the final structures of the MIM resonators.

For the MIM resonators, we used AZMIR-701 photoresist spun at 4000 rpm for 30 seconds and heated at 90°C for 1 minute. The laser lithography equipment uses a classical ultraviolet line, λ=365nm. The power and the writing speed were optimized to obtain the periods ($d = 12, 11, 10, 9\mu m$), while the resonator space was maintained constant fig.2.9(a). The resist was developed for 30 seconds with AZ726 MIF and rinsed in deionized H_2O. Prior to the eching of the layer, the resist is hardened at 110°C for 1 minute fig.2.9(b). The acid wet etching was conducted with a citric acid ($C_6H_8O_7$) and hydrogen peroxide (H_2O_2) solution with a 2:1 ratio at 20°C to define the resonator array fig.2.9(c,d). Dektak measurements showed a hight of $\sim$ 300nm, corresponding to a clear selective wet etching ratio between InAsSb and GaSb.

2.4.3 Scanning electron microscopy SEM characterization

To image the MIM resonator, scanning electron microscopy (SEM) measurements are applied to our structures. This method is an adaptable instrument that analyse and examine microstructures by scanning a sample with a focused electron beam. It delivers information about the samples' morphology, topography, and the chemical composition. When a sample is irradiated with a fine electron beam (called an electron probe), secondary electrons are emitted from the specimen surface. Topography of the surface can be observed by two-dimensional scanning of the electron probe over the surface and acquisition of an image from the detected secondary electrons. The SEM requires an electron optical system to produce an electron probe (i.e electron beam). The beam hist the sample where the detector collect the secondary electrons, then analysed in an operational system. Finally, an image is generated in a display unit. Figure 2.10 present images of the reflection measurements of four samples of different widths $w = 1.84 \pm 0.05\mu m$, $w = 4.3 \pm 0.2\mu m$, $w = 1.21 \pm 0.01\mu m$, $w = 2.89 \pm 0.01\mu m$ of the MIM antennas under normal incidence in a reduced area of $100\times100\mu m$.

2.4.4 Fourier transform infrared spectroscopy (FTIR)

The engineered MIM resonators are spectrally characterized using a FTIR in the spectral range between $(15-55\mu m)$. The IR radiation passes through the sample, some of the infrared radiation is absorbed, reflected, or transmitted.

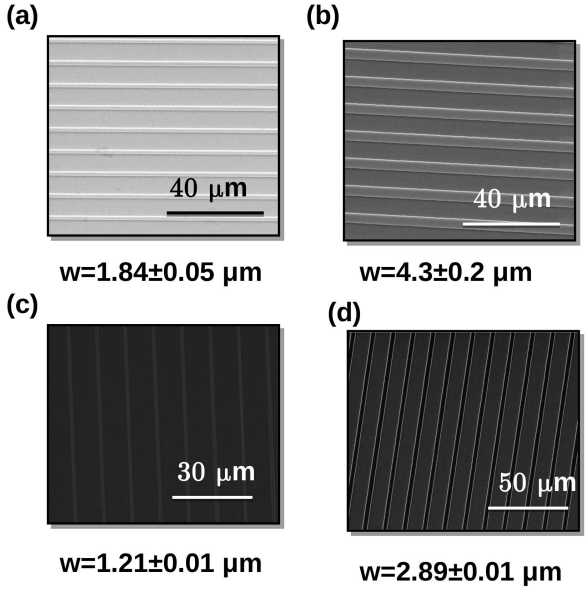

Figure 2.10: SEM images of the InAsSb:Si grating of (a) $w = 1.84 \pm 0.05\mu m$, (b) $w = 4.3 \pm 0.2\mu m$, (c) $w = 1.21 \pm 0.01\mu m$, (d) $w = 2.89 \pm 0.01\mu m$

All the reflectance spectra have been performed with Bucker V70 (FTIR) spectrometer equipped with KBr beam splitter, a far-infrared source and a Si-bolometer cooled at 4.2 K. The incident beam makes an angle of 60° with the normal of the surface since we use the Brewester mode setup for far-infrared experiment. A KRS holographic wire grid polarizer has been used to polarize the incident light.

2.5 Results and discussion

In this section we will discuss the results obtained from the experimental measurements, and compare them to the simulated models. Figure 2.11 shows the 35 zones or devices realized by MBE and laser lithography as presented before. Each large sample contains a collection of antenna samples with a specific period d, thickness h, and gap g. Notice that the parameter that differs is the width w which is mentioned for each sample with a statistical error calculated between the over-all widths of the antennas. Each sample is named by A, B, C, and D respectively, which in turn is divided into zones

named A1, B3, C5,..... each zone is subjected to the FTIR measurements by an incident beam that makes an angle of 60° with the normal of the surface, since the angle of incidence have do not affect the measurements as mentioned before fig.(2.3) . The absorption spectra were extracted from the reflectance measurements by considering the transmittance to be zero because of the back mirror.

Figure 2.11: Schematic of the 35 zones fabricated and divided in four portions A, B, C, and D. Each zone has an average value of the width of the antennas with error expressed in μm.

The absorption spectra extracted from the FTIR measurements for different samples (B3, B6, B8, D2, D4, A5, A6, and A2) are shown in Figure (2.12). The comparison between the simulated results (dashed curves) and the experimental ones (full lines) shows a very good agreement with a slight decrease in the experimental absorption due to geometrical imperfections. A summary of the result stating the resonant wavelength with the corresponding experimental and simulated width is arranged in table (2.1). More importantly, we notice that the increase in the width of the antennas shows a very clear shift in the resonant wavelength toward higher values.

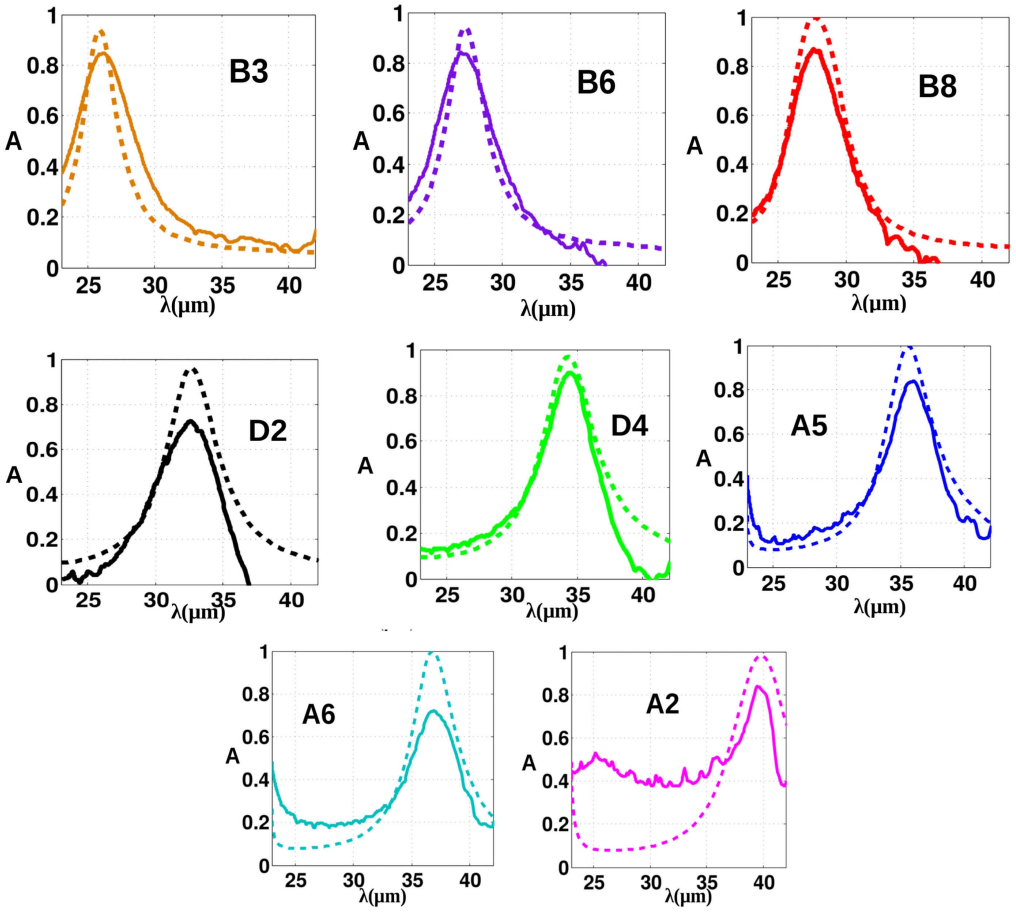

Figure 2.12: The comparison between the simulated results (dashed lines) and the experimental ones (full lines) for different width of the rods w.

In figure (2.13) we plot of the relation between the experimental and the simulated width w of the antennas as a function of the resonant wavelength λ_r .This follows a clear linear behaviour previously predicted by equation (2.6). The slope of the experimental graph allows to deduce the gap plasmon's effective index ($n_{eff} \simeq 4.7$) which in turn predict the approximate value of the theoretical thickness of the GaSb spacer for the samples.

Note that tuning the resonances of the gap plasmon mode by just changing the width of the antennas is an easy and reproducible step in the laser lithographic procedure. These results allow us to reach the subwavelength

	λ_r (μm)	w_{exp} (μm)	w_{sim} (μm)
B3	25.87	1.7 ± 0.22	1.9
B6	27.28	1.78 ± 0.91	2.05
B8	27.68	1.6 ± 0.18	2.1
D2	32.72	2.35 ± 0.32	2.6
D4	34.33	2.78 ± 0.08	2.78
A5	35.54	2.6 ± 0.15	2.9
A6	36.74	2.89 ± 0.09	3
A2	39.97	3.25 ± 0.14	3.3

Table 2.1: The resonant wavelength λ_r, the experimental w_{exp} and the simulated w_{sim} antenna width of selected zones

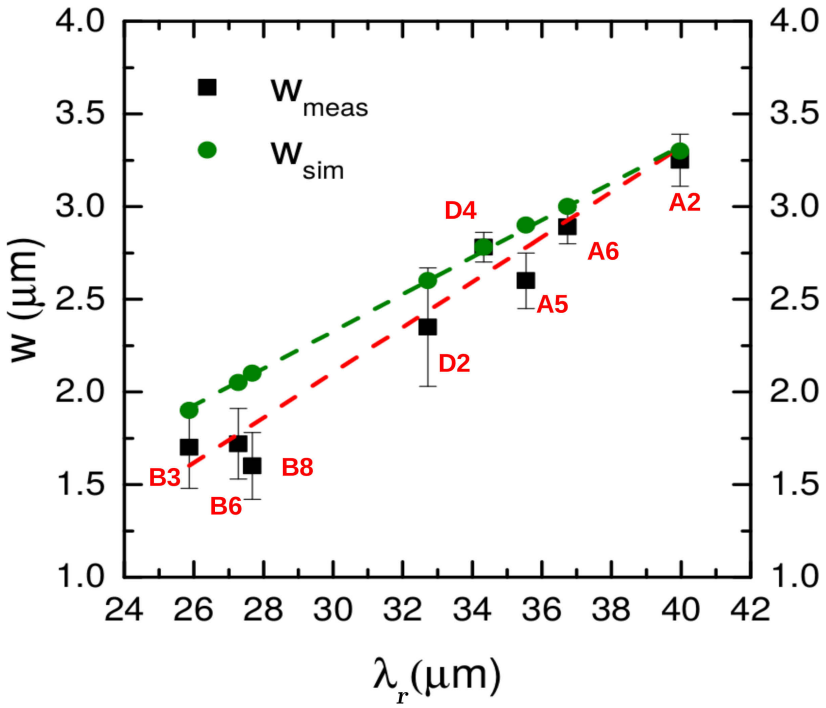

Figure 2.13: The linear behaviour of the resonant wavelength λ_r with respect to the width of the antennas w according to the experimental and simulated data.

scalability and tunability of HDSC MIM resonators in the THz range which can not be achieved using noble metals.

In order to compare the performance of the HDSC-based MIM antennas operating in the far-IR to those made of noble metals that operates in the visible range, we analyse the quality factor $Q = \lambda_r/\Delta\lambda$, where $\Delta\lambda$ is the full width at half maximum of the absorption line. The Q-factor is a qualitative characteristic of the MIM resonators which determines their efficiency and related to the absorption and scattering losses. First, both experimental and the simulated Q factors for the tested samples are close with an average error value less than 15%, see Table (2.2). These values are comparable with the state of art for MIM antennas made of noble metals [83, 84, 96]. Our results demonstrate that the electromagnetic properties of our HDSC-based MIM resonators are similar to their metallic counterpart and that gap plasmon resonances can be efficiently transposed in the far-IR.

	B3	B6	B8	D2	D4	A5	A6	A2
Q_{exp}	4.65	5.4	5.5	5.85	6.8	6.9	6.61	6.23
Q_{sim}	7.2	7.3	5.7	6.6	6.5	7.05	7.6	5.68

Table 2.2: The resonant wavelength λ_r, the width w of the samples B3, B6, B8, D2, D4, A5, A6, and A2 with the experimental ans simulated Q factors.

2.6 Conclusion

In this chapter, we have demonstrated theoretically and experimentally the potential of InAsSb:Si and GaSb materials to realize MIM antenna arrays which support gap-plasmon resonances up to THz frequencies ($\sim$ 7 THz). This approach allows us to reach near perfect absorption in the far-IR spectral range by easily adjusting the antenna geometry. The spectral positions of the gap plasmon resonances and their corresponding quality factors extracted from the absorption measurements in the far-IR are equivalent to those accomplished with noble metals in the visible range. These results show that HDSC-based MIM antennas are a flexible and CMOS compatible technology and might be a very significant improvement for various far-IR and THz applications such as sensing, imagery and security [155].

Chapter 3

Hyperbolic metamaterial wires

Metal-Insulator-Metal (MIM) resonators are a widespread plasmonic system that produce unprecedented sub-wavelength confinement and enhancement for the electromagnetic field. Both properties are highly desirable for many key technologies such as photovoltaics, lightening, biosensing, etc. In the previous chapter we studied the MIM resonators theoretically and experimentally without taking into consideration the effect of extremely decreasing their geometrical parameters in order to miniaturize them. In the slow light regime, these resonators are inefficient since they are unable to couple with the incident radiations. This limits the minimal size of the plasmonic resonators and thus the light confinement to one twentieth of the operating wavelength. In this chapter, we demonstrate that the use of Hyperbolic Metamaterials (HMs) instead of dielectric insulator allows to size down plasmonic resonators to only one hundredth of the wavelength while preserving a large optical efficiency. This miniaturization effect is explained by analyzing the slow modes supported by HM wires whose properties are driven by the proportion of dielectric and metal involved for their realization. We propose a simple model demonstrating that efficient hyperbolic wire antennas operate over a broad range of frequency and whose dimensions depend on the filling ratio in metal and dielectric.

Optical plasmonic nano-antennas offer fascinating ways to manipulate electromagnetic radiations at a deeply subwavelength scale [85]. Among the different geometries that have been considered, optical patch antennas, also known as Metal-Insulator-Metal (MIM) structures or gap-plasmon resonators, have in particular proven to be an efficient approach for many optical applications ranging from spectroscopy, light emission or biosensing to pho-

tovoltaics [86, 87, 88, 52, 53]. The geometry of a MIM resonator is extremely similar to that of microwave patch antennas, except for the ratio between the operation wavelength λ_r and the size of the patch. In the microwave range the typical width of the patch is $\lambda_r/2$, while optical patch antennas are much smaller than the wavelength because they operate close enough to the plasma frequency of metals and thus benefit from the plasmonic nature of metals.

3.1 MIM antennas and their limitations

A MIM antenna is constituted of a metallic patch separated from a metallic substrate by a dielectric spacer, Fig.3.1a. The properties of the antenna originate from the fact that a peculiar guided mode called gap-plasmon [4] propagates in the dielectric spacer of thickness g, along the metallic planes. This mode presents a very high effective index n_{gap}, and thus a very short effective wavelength. It can be approximated by the following equation:

$$n_{gap} = \sqrt{\epsilon_d}\sqrt{1 + \frac{2\delta_p}{g}} \tag{3.1}$$

where $\delta_p = c/\omega_p$ is the penetration depth into the metal and ϵ_d is the permittivity of the dielectric spacer [144, 94]. This mode is reflected by the edges of the patch, so that the structure forms an actual Fabry-Perot cavity, whose fundamental resonant wavelength is typically given by $\lambda_r = 2n_{gap}w$ where w is the size of the resonator [137]. The ratio between the size of the resonator and its operation wavelength is critical: it is directly linked to the ability of the resonator to concentrate light efficiently and to produce various phenomenon [90, 91]. It can be quantified by introducing a miniaturization parameter

$$\boxed{m_p = \frac{\lambda_r}{w}} \tag{3.2}$$

The effective index n_{gap} increases when the thickness g of the spacer decreases, as shown Fig. 3.1b, and so does the ratio m_p. For example, in references [95, 96] a ratio $m_p = 10$ is reached for nanocubes placed above a dielectric spacer presenting a subwavelength thickness of $\lambda/70$ in the visible, which represents only a few nanometers.

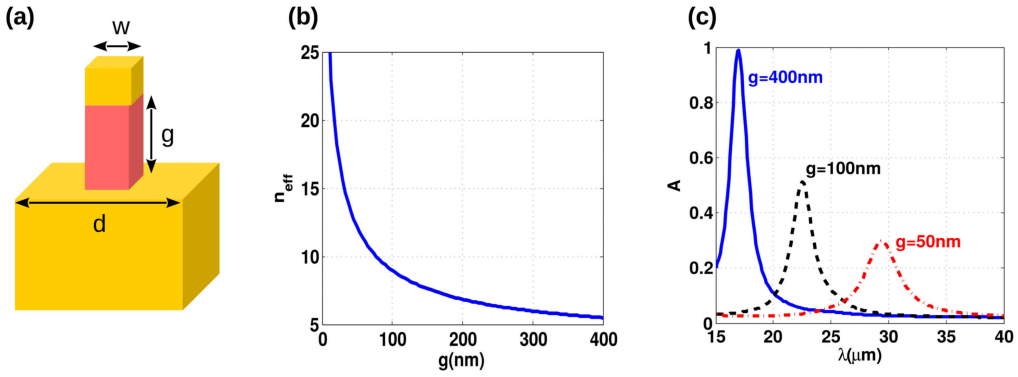

Figure 3.1: (a) A schematic of a cube MIM antenna. (b) Absorption curves of MIM antennas composed of InAsSb-GaSb-InAsSb for a period $d = 10\mu m$, a width $w = 3\mu m$, $h = 0.32\mu m$ and five different gap thickness $g = \{0.8, 0.5, 0.4, 0.3, 0.2\}\,\mu m$. (c) The effective index n_{gap} of the gap plasmon mode different dielectric spacer.

Beyond the simple miniaturization of resonators, high effective index gap-plasmons are accompanied by a slow light effect which is highly desirable to enhance light-matter interaction. Using high effective index modes is thus a strategy that allows to reach strong nonlinear response or achieving unheard of reduction for the lifetime of emitter placed under the patches [100, 101, 102]. This Purcell effect, giant as it may be, occurs when the gap g is very small and when the cavity is only barely coupled to the outside continuum - making the emitting device much less efficient that what could be expected. For instance, when ultra-thin spacers are considered, the incident light is unable to couple with the gap plasmon modes leading to an inefficient absorption, Fig.1c. To summarize, beyond a ratio m_p of typically 10 to 20 [103], the resonator becomes intrinsically inefficient.

Here we propose to reach both higher miniaturization ratios and higher efficiencies by replacing the dielectric spacer by a hyperbolic metamaterial (HM) layer, as shown Fig. 2. Such a HM spacer actually supports guided mode with even higher effective index than gap-plasmons, allowing to reach a miniaturization ratio of $m_p = 100$ - while staying much thicker, thus ensuring an efficient coupling to the continuum. We call these structures hyperbolic wire antennas.

As is common with patch antennas, 2D and 3D resonators share the same physical principles but do not have exactly the same overall optical

response. In a first part, we thus propose a thorough physical analysis of a 2D hyperbolic wire antennas and a model for the resonators that we compare to full simulations. In a second part, we extend our analysis to the full 3D case.

3.2 Effective properties of hyperbolic wires

Hyperbolic metamaterials are a class of artificial anisotropic materials that consist of a periodic metallo-dielectric structures presenting hyperboloid iso-frequency surfaces [105, 106, 107], hence their name.

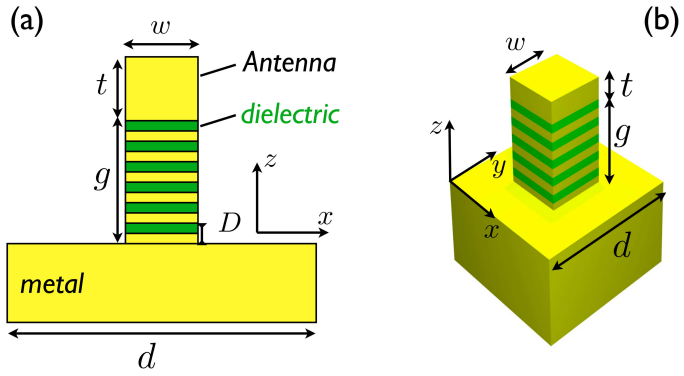

Figure 3.2: Schematic of the unit cell for a metallic pach suspended over a hyperbolic wire placed on a metallic subsrate. (a) and (b) corresponds respectively to the 2D and 3D cases.

When the period is much smaller than the wavelength, these multilayers behave as a homogeneous medium characterized by a effective permittivity tensor $\bar{\epsilon}$ whose principal elements are ϵ_x, ϵ_y and ϵ_z. Two kinds of HMs have to be distinguished. Type I HMs present a negative permittivity in the extraordinary direction ($\epsilon_z < 0$) and positive permittivities in the ordinary directions ($\epsilon_x > 0$ and $\epsilon_y > 0$). Meanwhile, type II HMs have one dielectric-like component ($\epsilon_z > 0$) and two metallic-like components ($\epsilon_x < 0$ and $\epsilon_y < 0$). Nano-wires, gratings or multi-layers based structures are the main approaches allowing to design both types of HMs [108, 109, 110]. Stacks of metallic and dielectric films have in particular been considered for realizing flat lenses [111, 112] and absorbers or polarisers when an additional

structuring is employed [113, 114, 115]. A rainbow trapping effect has been demonstrated with tapered HMs of type II supporting slow guided modes propagating in the extraordinary direction where $\epsilon_z > 0$. Their broad spectral response is due to the varying width of those tapered waveguides between a tens to a quarter of the incident wavelength [116]. Here, a metallo-dielectric multilayer belonging to the type II category is also considered but the miniaturization effect is obtained for modes guided in the ordinary direction (i.e. perpendicular to the z-direction). We demonstrate that similarly to MIM patch antennas, these modes recognized as BPPs resonate in a cavity whose width is determined by their effective index [104, 110, 117].

We consider a 2D metallic patch of width w and thickness t placed on top of a hyperbolic wire which consists of periodic stack of metal and dielectric layers with respective thicknesses and permittivities (h_m,ϵ_m) and (h_d,ϵ_d), as shown Fig. 2a. Note that the metallic patch and substrate are made with the same metal of permittivity ϵ_m. The dielectric filling factor is defined by $\rho = h_d/D$ where D is the lattice period of the multilayer ($D = h_m + h_d$). This theoretical study actually holds for any medium that can be described by the Drude model, whether it is a metal, strictly speaking, or a highly doped semiconductor. Here we consider InAsSb, a highly doped semiconductor whose plasma frequency can be tuned by playing with the doping concentration. In that case, the plasma frequency is in the infrared. The hyperbolic behaviour of the multilayer can thus be expected to occur only below the plasma frequency. This material is in addition compatible with CMOS technology and its relative permittivity is given by a $\epsilon_m = \epsilon_\infty(1 - \omega_p^2/(\omega(\omega + i\gamma)))$ with $\epsilon_\infty = 11.7$, $\omega_p = 351.10^{12}\ rad.s^{-1}$ and $\gamma = 10^{13}\ rad.s^{-1}$ [65, 118, 119]. The dielectric between the InAsSb layers is GaSb, a dielectric whose permittivity $\epsilon_d = 13.4$ can be considered constant [120].

For p-polarized light (the magnetic field being perpendicular to the x-z plan) and in the long wavelength limit ($\lambda >> D$) the multilayer behaves as a homogeneous anisotropic medium, characterized by a permittivity tensor whose relative principal elements are given by

$$\varepsilon_\perp = (1 - \rho)\varepsilon_m + \rho\varepsilon_d \tag{3.3}$$

$$\varepsilon_z = \left(\frac{1 - \rho}{\varepsilon_m} + \frac{\rho}{\varepsilon_d}\right)^{-1} \tag{3.4}$$

with $\varepsilon_x = \varepsilon_y = \varepsilon_\perp$. Within the HM, electromagnetic waves thus satisfy

the dispersion relation:

$$\frac{k_x^2}{\varepsilon_z} + \frac{k_y^2}{\varepsilon_z} + \frac{k_z^2}{\varepsilon_x} = k_0^2 \tag{3.5}$$

where k_0 is the wavenumber in vacuum. To understand the optical properties of HWs, we first analyze the guided modes propagating in a 1D waveguide made of two metallic planes filled by a HM of type II ($\epsilon_z > 0$ and $\epsilon_\perp < 0$). The structure presented in the inset of Fig. 3b is invariant in the y and x directions, while perfect boundary conditions are assumed for $z = 0$ and $z = g$. Looking for guided modes propagating in the ordinary x direction, a straightforward calculus leads to conclude that several modes can be supported by the waveguide, characterized by an integer m, the order of the mode. The magnetic field associated with the m^{th} guided mode (for p polarization) can be written

$$H_y^{(m)} = H_0 \cos\left(m\frac{\pi}{g}z\right) e^{-ik_x^{(m)}x} \tag{3.6}$$

where $k_x^{(m)}$ is the propagation constant along the x-direction and H_0 its (arbitrary) amplitude. Using Eq.(3.5), the effective index of the m^{th} mode defined by $n_{eff}^{(m)} = k_x^{(m)}/k_0$ is then given by:

$$n_{eff}^{(m)} = \sqrt{\epsilon_z}\sqrt{1 - \frac{1}{\epsilon_\perp}\left(\frac{m\lambda}{2g}\right)^2}. \tag{3.7}$$

This result shows that the effective index of a guided mode is mostly driven by the value taken by the extraordinary permittivity ϵ_z. This quantity is shown on Fig. 3.3a as a function of the wavelength for different values of ρ, the dielectric filling ratio. The real part of ϵ_z presents a maximum that red-shifts and reaches very high values when the filling ratio decreases – offering to control and to tune this crucial parameter. Figure 3.3b shows the effective indices given by Eq.(4.18) reached by the three lowest order guided modes propagating inside a $g = 2\,\mu m$ wide waveguide. For the lossless metallic case, these high-k guided modes, which can be connected to bulk hyperbolic plasmons [110, 117], present a maximal effective index at the effective frequency ω_{eff} obtained when $\epsilon_z \to +\infty$:

$$\omega_{eff} = \omega_p \left(1 + \frac{(1-\rho)}{\rho}\frac{\epsilon_d}{\epsilon_\infty}\right)^{-1/2} \tag{3.8}$$

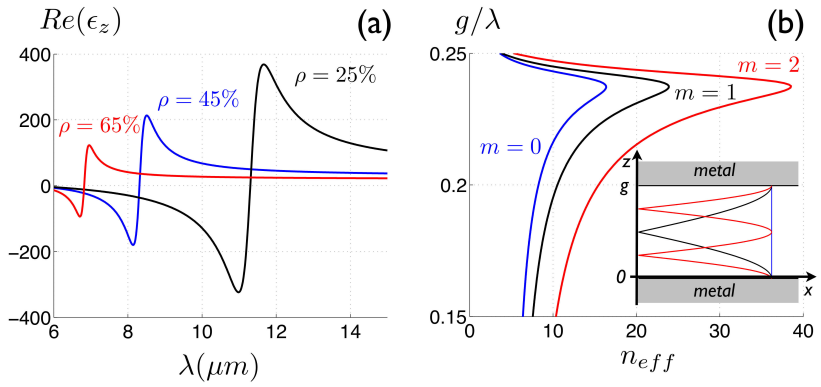

Figure 3.3: (a) Real part of ϵ_z as a function of the wavelength and for 3 compositions ρ of 25%, 45%, 65%. (b) Dispersion relation of the 3 first modes ($m = 0, 1, 2$) as a function of the reduced frequency g/λ. The inset represents the modulus of the magnetic field (Eq. (3.6)) associated with the three lowest order modes in a $g = 2\mu m$ wide waveguide. Blue, black and red modes correspond respectively to $m = 0, 1, 2$.

This result is in agreement with the redshift observed for the maximal $\Re(\epsilon_z)$ at the effective wavelength $2\pi c/\omega_{eff}$ when ρ decreases, Fig. 3a. Since the resonant frequency of HWs arises in the slow light regime i.e. close to the effective frequency, we are able to derive the theoretical size reduction of a resonator sustaining the m^{th} resonance: $m_p^{(m)} = 2Re(n_{eff}^{(m)}(\omega_{eff}))$. The miniaturization parameter for that HW supporting the fundamental TEM mode (which resemble to the fundamental BPP mode [104]) is hence given by:

$$m_p^{(0)} = 2\Re\left(\sqrt{\epsilon_z(\omega_{eff})}\right) \tag{3.9}$$

By decreasing the amount of dielectric material in the composition of the HW, the resonance is shifted over a broad range of frequency – while the wire is drastically miniaturized, as shown Fig. 4. For a very small filling fraction of dielectric about 1%, it is predicted that the fundamental resonant wavelength is more than one hundred times larger than the width of the HW, thus exceeding the usual limit imposed to MIM resonators, Fig. 4b.

This simple physical picture is validated by comparing the response of composite HW to the response of a patch antenna in which the multilayer is replaced by a spacer made of an equivalent homogeneous hyperbolic medium,

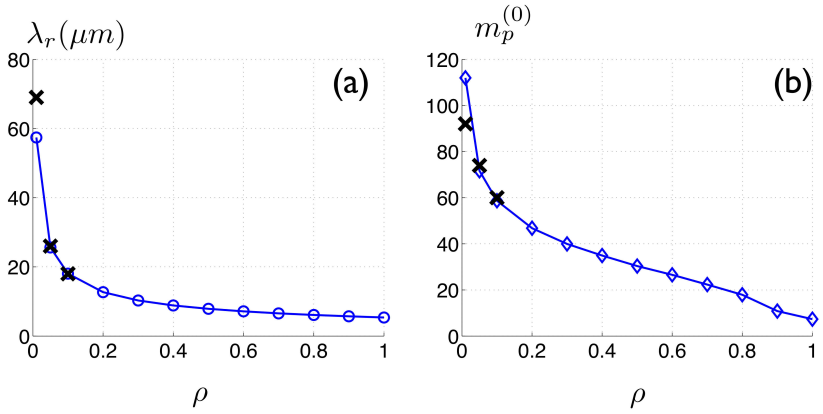

Figure 3.4: (a) Theoretical resonant wavelength of the HW for the fundamental mode as a function of the filling ratio in dielectric ρ. (b) Miniaturization factor given by Eq.(3.9) for a HW resonating with the fundamental mode as a function of ρ. Black crosses correspond to the results obtained for the 3D simulations.

Fig. 5. Here, we still consider the 2D case depicted on Fig. 2a where the antennas are periodically settled in the x-direction with a pitch $d = 1\,\mu m$. For a filling factor $\rho = 45\%$, the theoretical fundamental resonant wavelength is found around $\lambda_r^{(0)} = 8.5\,\mu m$ where $\Re(\epsilon_z)$ attains its maximal value of 213, Fig. 3a. According to Eq.(3.9), the width of the metallic patch is chosen to $w = 300\,nm$ for a thickness $t = 350\,nm$. The heigh of the HW is $g = 2\,\mu m$ and it is made of 40 metallic and dielectric films of respective thicknesses $h_m = 27.5\,nm$ and $h_d = 22.5\,nm$. The absorption spectra are calculated with a finite element method solver (Comsol Multiphysics) when the structure is illuminated by a plane wave in normal incidence with a magnetic field oriented in the invariant y-direction (p-polarization), Fig. 5a. A good agreement is observed for the absorption spectra as well as for the magnetic field maps, Fig. 5b. It appears three resonances associated to the fundamental mode TM_0 (at $\lambda = 8.7\,\mu m$), the first odd mode TM_1 (at $\lambda = 9.5\,\mu m$) and the second even mode TM_2 (at $\lambda = 11.2\,\mu m$). The spatial extensions of these resonant modes agree with BBP modes obtained for the HM waveguide depicted in the inset of Fig. 3b . We also notice that the calculated resonant wavelength for the fundamental mode is close to the theoretical one $\lambda_r^{(0)} = 8.5\,\mu m$.

These results obtained when the HWs are ended by a metallic patch whose

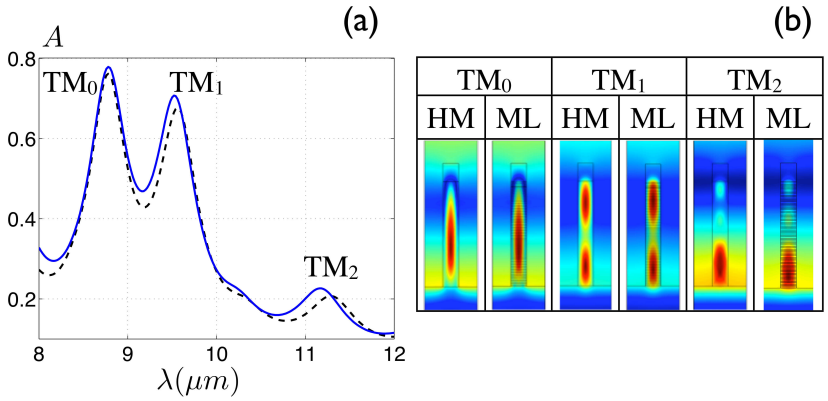

Figure 3.5: (a) Absorption spectrum calculated for a metal-dielectric multilayer spacer (solid curve) and for an homogeneous HM spacer (dashed curve). (b) Modulus of the magnetic field calculated for the 3 first resonant modes. The columns labelled HM and ML correspond respectively to a homogeneous HM spacer and a multilayer one.

thickness $t = 350\,nm$ exceeds the penetration distance for the waves into the metal (about 200 nm) demonstrate that the resonances at work inside HWs are based on stationary BPP modes resonating in the ordinary x-direction. However, similar properties are obtained when the metallic patch is removed. Its presence is nevertheless convenient because it allows to analyze the HW in terms of guided modes having effective indices given by Eq. (4.18). We also notice that if BPP modes can be coupled to radiative waves by a grating deposited above a uniform HM layer as for hypergrating structures [114], the miniaturization effect observed for a HW originates from the formation of stationary BPP waves confined in a cavity whose width is determined by Eq. (3.9). More generally, a stronger miniaturization effect is seen for HWs than for isotropic metallic wires. The latter support localized surface plasmon resonances along or at their top end according to the geometry [121, 122]. For similar structures consisting of a periodic set of metallic nanorods standing on a metallic plate, the electric field enhancement is associated to an absorption efficiency of 90% for a miniaturization factor about 25 which is 4 times smaller than that for HWs [123]. Even if the control the spectral properties of nanowires is envisaged by adjusting the doping level of semiconductors [124, 125], HMs offer an original alternative to synthesize at demand highly miniaturized nanowires made of predetermined dielectric and metallic mate-

rials.

3.3 3D simulations of hyperbolic wires

We now extend the previous results to the case of 3D HWs periodically arranged in a square lattice in the x-y plane with a pitch d in both directions. We focus in particular on small dielectric filling factors in order to conceive highly miniaturized HWs. The period of the multilayer is chosen to be $D = 100\,nm$ while ρ is decreased from 10%, 5% to 1%. For each case the thickness g, the period d and the width w of the wires are optimized to get an absorption efficiency higher than 90% attributed to the resonance of the fundamental BPP mode. Remark that the thickness of the metallic patch is kept constant to $350\,nm$ in these 3D electromagnetic simulations realized with a home-made code based on the RCWA method [80]. The absorption spectra calculated in normal incidence show a shift for the fundamental resonance wavelength from $18\,\mu m$ to $69\,\mu m$ when the filling factors is varied for $\rho = 10\%$ to $\rho = 1\%$, Fig 6a. The geometrical parameters and miniaturization parameter obtained for these different filling ratios are summarized in Table 3.1.

ρ	$d\,(\mu m)$	$g\,(\mu m)$	$w\,(nm)$	$\lambda_r(\mu m)$	$m_p^{(0)}$
10%	0.4	2	300	17	60
5%	0.5	3.5	350	26	74
1%	1.4	10	750	69	92

Table 3.1: Geometrical parameters, resonant wavelengths and miniaturization parameter for 3D hyperbolic wires presenting three metal-dielectric composition ρ.

Highly miniaturized HWs presenting a large aspect ratio g/w might be challenging from the fabrication point of view. However, complex structures such as thick photonic crystals reaching aspect ratios about 4 have already been fabricated with a time-multiplexed etching process [126, 127]. Moreover, the current molecular beam epitaxy (MBE) process allows the deposition of multilayers whose thicknesses are controlled at the monoatomic resolution i.e. for a $0.3\,nm$ typical error. Since HWs work in the homogenization regime, their optical properties are robust against these small fluctuations even in the extreme miniaturization regime.

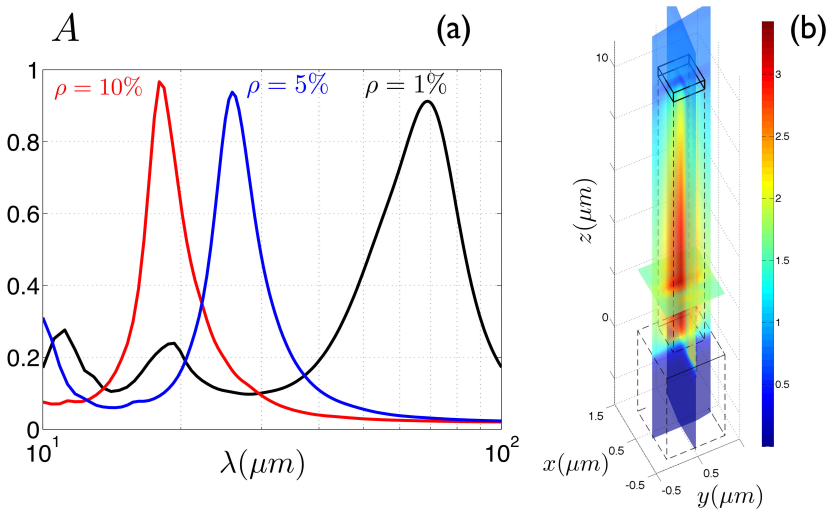

Figure 3.6: (a) Absorption spectra in a logarithm scale calculated for three hyperbolic wires of filling ratio in dielectric $\rho = \{1\%, 5\%, 10\%\}$ (respectively the black, blue and red curves). (b) Modulus of the magnetic field for $\rho = 1\%$ at the resonant wavelength $\lambda = 69\mu m$.

In this latter case, for $\rho = 1\%$, the 3D map of the magnetic field modulus plotted in Fig. 6b at $\lambda_r = 69\,\mu m$ proves that the resonant absorption can actually be attributed to the fundamental BPP mode. The resonant wavelength and the miniaturization parameter obtained for these 3D simulations are compared in Figure 4 to the theoretical calculations obtained with the effective model developed in paragraph II. The good agreement between these results demonstrates that our simple picture is still valid for 3D structures, and that the resonant wavelength can be shifted over a broad range of wavelength by controlling the composition in dielectric of the hyperbolic metamaterial. We underline that the width of the HW is reduced to only one hundredth of the resonance wavelength (one order of magnitude smaller than for a MIM resonator), while preserving a large efficiency. The absorption is actually almost perfect whatever the resonance wavelength, which is very different from what occurs for regular MIM structures. Let us finally remark that similarly to MIM antennas, the fluctuation of the HW width should result in a broadening of the absorption line [96].

3.4 Conclusion

We have thoroughly studied the electromagnetic response of hyperbolic wires made of a highly doped semi-conductor and a dielectric material. We have provided a simple yet very accurate physical picture of their behavior, showing that BPP modes having very high effective indices can be squeezed inside deeply subwavelength resonators. This leads to an extreme miniaturization of HWs to only one hundredth of the wavelength while maintaining a very high absorption efficiency. The modification in their dielectric and metallic fractions provides a versatile way to shift the absorption line over a wide range of wavelength $[10 - 100]\mu m$. Thanks to this physical analysis, we are confident that HWs can be used in other frequency ranges and with other materials (like noble metals). Since the design we propose allows to overcome the major limitations of standard plasmonic resonators such as MIM or nanowires antennas, we hope hyperbolic wires will be useful for numerous applications.

Chapter 4

Universal metamaterial absorber

The control of light absorbance plays a fundamental role in today's photonics technologies with strong impacts for solar energy harvesting or for light emitting and sensing components [128, 129, 130]. Since according the Kirchhoff's law, perfect absorbers and emitters are equivalent, significant efforts are pursued to realize compact artificial materials presenting an almost perfect absorption in a selective spectral range, for any polarization or incidence angle [131, 132, 133]. Whatever the approaches considered based either on critical coupling or impedance matching effects, the targeted operating frequency usually imposes the choice of the materials constituting the absorbers and also strongly constraints the design. These limitations originates from the intrinsic nature of Maxwell's equations that are invariant under a change of scale solely for non-dispersive materials. However, realistic materials are always dispersive and simple scaling laws can't be applied to tackle the variation of the absorption loss. For example, plasmonic absorbers have proven to be effective for visible and infrared radiations while metamaterials are preferably used from the terahertz to the microwaves [134, 135, 138, 139, 140]. Another approach consists of modifying the materials property such as its plasma frequency according to the targeted operating frequency [65, 141, 142, 143]. For those relying on the critical coupling condition, the minimum size of the resonators is always larger than $\lambda/20$ despite the strategies involved to reduce the effective wavelength of the mode responsible for the resonance [96, 144].

In this chapter we propose a resonant absorber which is universal since

its optical properties are independent from the choice of the metals and dielectrics involved for its realization. The absorption frequency is demonstrated to be tuned from infrared to microwave frequencies by following simple scaling laws for universal absorber made of noble metal or highly doped semiconductors. In both cases, perfect absorption is reached for incident angles up to 30° and for any polarization of light. The universal absorber is in addition demonstrated to support a Fabry-Perot (FP) builds up in a near-zero dielectric thickness of $\lambda/100$ leading to an ultra-thin structure. This resonance is activated by a funnelling effect through slits of few nanometers wide, with a ratio of the period to the width of the slits that can easily be larger than 30,000.

4.1 Simple design absorbers and their limitations

Before demonstrating the concept of universal absorbers, in this section we will show the barriers encounters us from obtaining a tunable design that can perfectly absorb light over a wide range of frequencies. The starting geometry is a simple structure in which a dielectric layer of thickness l and a refractive index $n_d = n + i\kappa$ is backed with a perfect electric conductor (PEC), Fig 4.1(a).

The optical properties of this system can be understood from basic electromagnetic derivations of a lossless dielectric layer ($\kappa = 0$). Using transverse magnetic polarization in normal incidence and taking into account the PEC back mirror, the magnetic field inside the dielectric layer reads $H_z = Bcos(k_0 n_d y)$, with $k_0 = 2\pi/\lambda$. The electromagnetic continuity conditions applied at the interfaces leads to the classical $\mathbf{T}$ matrix that link the incident and reflected fields to the field inside the dielectric layer:

$$\begin{pmatrix} I \\ R \end{pmatrix} = \mathbf{T} \begin{pmatrix} Bcos(k_0 n_d l) \\ B\frac{k_0}{in_d} sin(k_0 n_d l) \end{pmatrix} \tag{4.1}$$

Here $\mathbf{T}$ is the matching matrix (i.e Passage matrix) between the air and the dielectric layer and can obtained from the boundary conditions applied to the system:

$$\mathbf{T} = \frac{1}{2} \begin{pmatrix} 1 & \frac{n_d}{k_0} \\ 1 & -\frac{n_d}{k_0} \end{pmatrix} \tag{4.2}$$

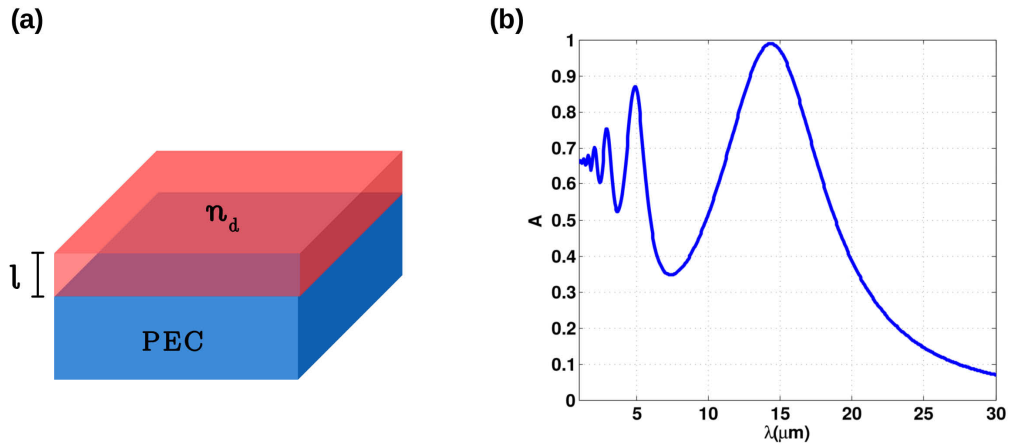

Figure 4.1: (a) Configuration for a lossy dielectric slab backed by a PEC. (b) absorption line of a dielectric slab of $l = 1\mu m$ and $n_d = 3.7 + 0.5i$

Now, the amplitude of the magnetic field in the slab can be expressed in a conventional formulation:

$$B = \frac{2\tau}{1 + \rho e^{2ik_0 n_d l}} I \tag{4.3}$$

Where $\rho = (n_d - 1)/(n_d + 1)$ is the classical Fresnel reflection coefficient and $\tau = 2n_d/(1 + n_d)$ is the transmission coefficient. The electromagnetic field inside the layer is thus enhanced when the denominator of equation (4.3) vanishes. This gives the usual Fabry-Perot resonance conditions:

$$1 + \rho e^{2in_d k_0 l} = 0 \tag{4.4}$$

The first condition, $\mid \rho \mid = 1$ can be approached when the absorption coefficient is weak ($\kappa \ll n$) and when $n \gg 1$. The second one is a phase condition which implies that the mode is build up inside the dielectric layer:

$$2nk_0 l + \phi_{TM} = (2p + 1)\pi \tag{4.5}$$

where $p = 0, 1, 2, ...$ so $2p+1$ is an odd integer, and $\phi_{TM} = \arg(\rho) = 0\ [2\pi]$ for a lossless material as shown in the phasor diagram fig.4.2(a). In the case of perfect phase balance, destructive interferences between the incoming and the reflected waves arise leading to the phase condition obtained from eq.(4.5):

$$\boxed{l = \frac{\lambda}{4n}(2p + 1)} \tag{4.6}$$

So using relation (4.6) and choosing a quarter-wave layer the reflected wave is vanished which in turns maximize the absorption, and no absorption resonance exist for a layer thinner than the thickness l. Note that in the case of a transverse electric polarization TE the phase condition is $2nk_0l+\phi_{TE} = 2m\pi$ where ϕ_{TE} is a negative phase and m is an even integer. So that the relation between ϕ_{TE} and ϕ_{TM} can be written as follows:

$$\boxed{\phi_{TM} = \phi_{TE} + \pi} \tag{4.7}$$

The first attempt to obtain dielectric layers smaller than the ratio $\lambda/4n$ is to use a dielectric layer having high losses. These additional losses in the dielectric are added such that the interface reflection and transmission coefficient can be modified, which in turn unbalance the phase condition stated in eq.(4.5). This modification will effect ϕ_{TM} the reflection phase at the air-dielectric interface that will no longer equal to zero ($\phi_{TM} \neq 0$) fig.4.2(b). So to re-obtain the phase balance in eq.(4.5), the losses introduced in the dielectric layer will lead to increase the ϕ_{TM} that will balance the phase condition which in turn cause a reduction of size in the dielectric layer.

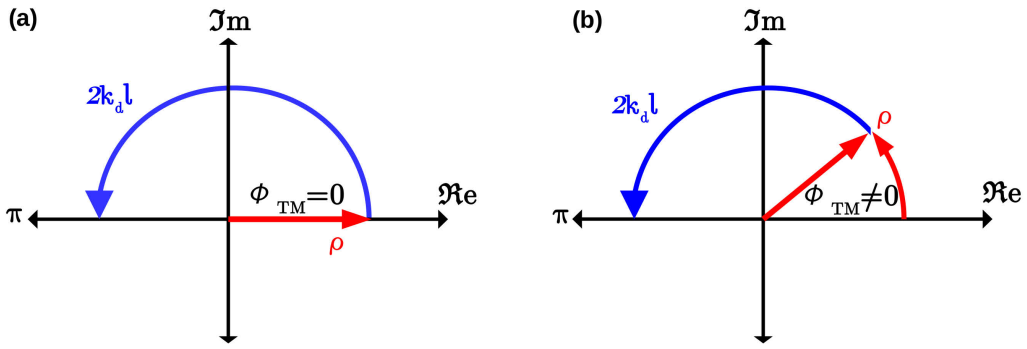

Figure 4.2: (a) Phasor diagram demonstrating the reflection coefficient ρ at the air-dielectric (lossless) interface is real so it generate a phase ϕ_{TM} of 0 $[2\pi]$. (b) Demonstrate that for a lossy dielectric a small phase shift is introduced $\phi_{TM} \neq 0$.

To demonstrate the results of this approach, we calculate the absorption spectra in TM polarization at normal incidence for a dielectric slab of thickness $l = 1\mu m$ and refractive index $n_d = 3.7 + 0.5i$ the perfect absorption is obtained at $14.9\mu m$ fig.4.1(b). This resonance satisfies the phase condition of equation (4.5) which is illustrated in fig.4.3(a) and occurs for a specific

value of the real n and the imaginary part κ of the dielectric layer and for other values the efficiency of the absorption decrease drastically as shown in Fig.4.3(b). This shows that the thickness of the absorber is dictated by the refractive index of the layer and though the real and the imaginary parts of the index. Indeed, Kats and co-authors in ref.[139] uses the attempt of tuning

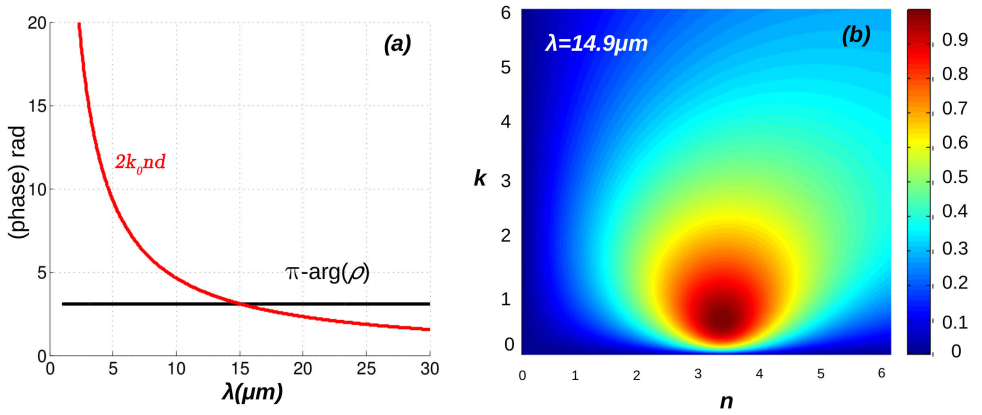

Figure 4.3: (a) The red curve is the phase inside the dielectric layer and the black curve is phase at the interface between the dielectric and the free space. (b) Map of the calculated absorption as a function of n and κ, the real and imaginary part of the complex refractive index n_d of thickness $l = 1\mu m$ for $\lambda = 14.9\mu m$, the absorption is perfect for $n_d = 3.7 + 0.5i$.

the phase by increasing the imaginary part of the dielectric layer with vanadium dioxide (VO_2) on a sapphire substrate. A ratio of $\lambda/65$ is obtained but this way faces an important limitation since this phase is tuned by temperature which is a very strict way, and the materials used always imposes the range of the frequency we are dealing with. Also the same author in ref.[138] utilizes the semiconductor Ge with high absorption on a gold substrate Au. This study is performed to introduce additional phase shift generated from the PEC mirror by using this structure at a specific wavelength when the conductivity of the Au substrate is finite. So instead of the phase of ρ_1 at the air-Ge interface we will have additional phase from ρ_2 at Au-Ge interface fig. (4.4). The combination of these two phases will introduce a large phase that can decrease the thickness for 20 nm which present a ratio of $\lambda/35$. These approaches are pretty useful and they can trap visible light in tenth of nanometers, but still the approach of the absorbing media face a lot of limitations. First, the refractive index and the absorption coefficient of a

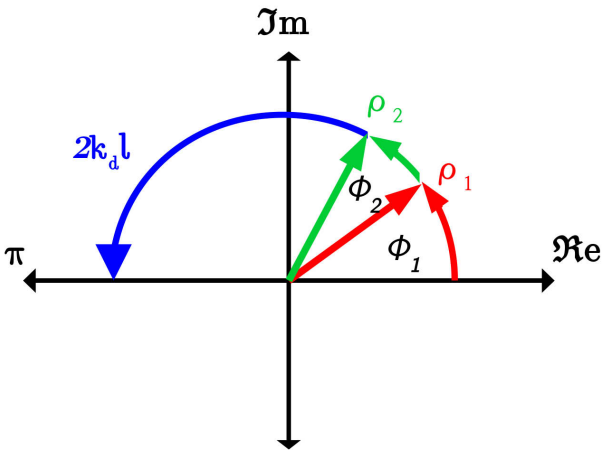

Figure 4.4: Phasor diagram demonstrating the phase of the reflection coefficient ρ_1 and ρ_2 at air-dielectric and dielectric-PEC interface respectively.

material must respect the Kramers-Kronig law, which in practice difficult to fully satisfy the FP conditions even for a quarter-wave layer. Second, extending the response for any wavelength is a hard task because of the material dispersion which prevent tuning the resonant frequency without changing the materials. Third, finding the proper materials that match in the growth technique and suitable for the fabrication process is a challenge. Fourth, the absorbers are still large in size and can not be integrated more using the same geometry. Finally, the efficiency of the design decreases when changing the incident angle and therefore becomes polarization dependent.

All the previous limitations made us think in a new way to overcome the challenges imposed by the materials used in realizing integrated perfect absorbers.

4.2 Design of the super absorber

From the simple absorber structure, we will describe our proposed universal absorber and its originality. This absorber consists of a deeply subwavelength periodic grating of pitch d made of nanometers slits of thickness h and width f etched in a thin metallic slab which is separated from a metallic back mirror by a dielectric spacer of thickness g as shown in figure 4.5(a). The main property of this design is that perfect absorption can be attained over a wide

range from infrared to microwave frequencies regardless of the materials used (i.e the metal and the dielectric). This total absorption can be tuned easily by modifying the geometrical parameters of the structure such as the period, the width of the slits or the thickness of the dielectric layer. In addition to the flexibility of the universal design, the integrated size of the structure adds a very important advantage to our approach since the resonant wavelength is trapped in the dielectric spacer of thickness $g = \lambda_r/100$. For example figure 4.5 (b,c) shows respectively the absorption spectra of two structures made of highly doped semiconductor (InAsSb) and silver (Ag) with GaSb as a dielectric spacer. Perfect absorption is achieved around $\lambda_r = 80\mu m$ for both materials using the following parameters $d = 2\mu m$, $g = 0.85\mu m$, $h = 0.32\mu m$, and $f = 10nm$ for InAsSb, and for silver (Ag) $d = 5.42\mu m$, $g = 1.078\mu m$, $h = 20nm$, and $f = 10nm$. These geometrical parameters obey the scaling laws that will be derived in the following sections. These fascinating properties can be understood and compared to the model explained in the first section. Where the goal is to introduce a phase shift in order to decrease the thickness of the dielectric layer, however in the universal design a huge phase is introduced and can be tuned by the geometrical parameters.

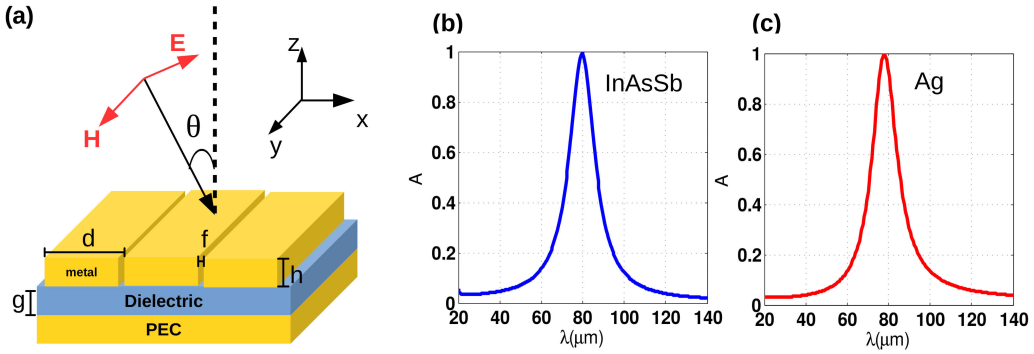

Figure 4.5: (a) represent the metamaterial absorbers made of a grating of thin slits of width f and thickness h periodically etched (pitch d) in a metal, a dielectric spacer of thickness g and a mirror. (b) and (c) are the absorption curves of the same structures but using different materials, InAsSb and Ag respectively.

4.3 Theory

To derive a theoretical model to the universal structure, we consider a 1D periodic set of slits of width $f = 10\ nm$ etched in the x-direction, with a pitch $d = 2\ \mu m$ and a thickness $h = 320\ nm$ for the metamaterial layer. This grating layer is considered to be InAsSb which is a highly doped semiconductor whose plasma frequency can be tuned by playing with the doping concentration. This material is in addition compatible with CMOS technology and its relative permittivity is given by a Drude model:

$$\varepsilon_{InAsSb} = \varepsilon_\infty \left(1 - \frac{\omega_p^2}{\omega(\omega + i\gamma)}\right) \tag{4.8}$$

with $\varepsilon_\infty = 11.7$, $\omega_p = 351.10^{12}\ rad.s^{-1}$ and $\gamma = 10^{13}\ rad.s^{-1}$ [65, 118]. The second layer is the dielectric spacer, of thickness g, filled with a GaSb insulator (that is assumed to be non-dispersive) of refractive index $n_d = 3.7$. Finally, at the bottom of the structure a substrate of InAsSb acts as a back mirror.

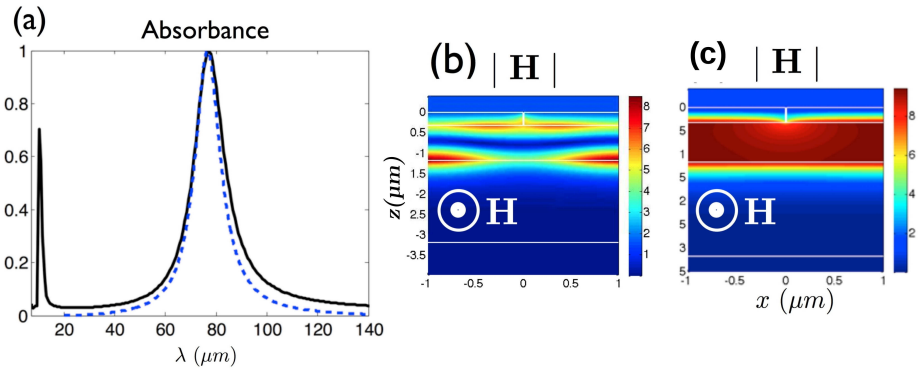

Figure 4.6: (a) Absorbance for a 1D metamaterial absorber ($f = 10\ nm$, $d = 2\ \mu m, g = 850\ nm$). The solid and dashed curves are respectively obtained with the exact electromagnetic simulation and with the equivalent dielectric model. (b) and (c) Maps of the modulus of the magnetic fields corresponding to $\lambda_s = 11\ \mu m$ and $\lambda_r = 77\ \mu m$ respectively.

The absorbance A is deduced from the energy reflection coefficient R computed using the Rigorous Coupled-Wave Analysis (RCWA) [80]. Two absorption lines are observed in normal incidence on the computed absorption

spectrum, for p-polarization case (*i.e.* a magnetic field along the slits in the z-direction), Fig. 4.6 a. The lower resonant wavelength, $\lambda_s = 11\ \mu m$, corresponds to a cavity-like mode localized into the slits, fig.4.6 (b). While the second absorption line at $\lambda_r = 77\mu m$ indicates that it can be assimilated to a symmetric Fabry-Perot resonance localized inside the dielectric spacer Fig. 4.6(c).

4.3.1 First homogenization: effective index of the grating layer

The first step to understand the physics of our structure and to derive the scaling laws is to find a simple analytical formula of the effective index for the metallic grating layer. For that purpose, the first layer can be replaced by an effective dielectric slab at the top fig4.7(a). Similarly to the case of Extraordinary Optical Transmission (EOT) [145], a gap-plasmon is excited and reflected at the top and at the bottom of the grating layer. Its complex effective index can be written as:

$$\bar{n}_{slit} = n_{slit} + i\kappa_{slit} \tag{4.9}$$

which presents a real part that is well approximated by:

$$\boxed{n_{slit} = \sqrt{1 + \frac{2\delta_p}{f}}} \tag{4.10}$$

where $\delta_p = c/\omega_p$ is the penetration depth into the metal [144, 94]. The resonant condition for the slit reads $\lambda_s = 2n_{slit}h + \lambda_\Phi$ where λ_Φ is a phase shift linked to the reflection coefficient of the gap-plasmon inside the metamaterial layer [146, 147]. Remark that the spectral position of this slit mode is insensitive to an increase of the period since each the gap plasmon are assumed to be not coupled to their neighbours.

Recently, different homogenization techniques for plasmonic systems had been used such as the methods in references [112, 148, 149, 150, 151] which are very effective for metal-dielectic multilayers or randomly distributed nanoparticles. However, when the gap plasmon mode dictates the optical response of the structure, it is very convenient to use the approach of ref. [152] that makes the equivalence of the metallic grating to an effective dielectric slab of complex refractive index $\bar{n} = n + i\kappa$ and thickness $\bar{t}$, Fig.4.7(a). The

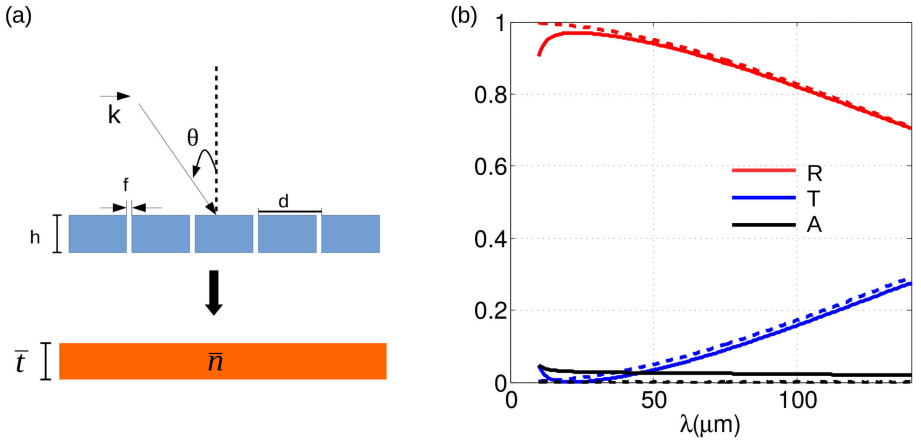

Figure 4.7: (a) schematic representation of InAsSb grating and an equivalent layer with the same optical response of thickness $\bar{t}$ and effective index $\bar{n}$. (b) Reflection, transmission, and absorption spectrum of a grating layer of ($d = 2\mu m$, $h = 0.32\mu m$, $f = 10nm$) of the grating layer (solid line) and the equivalent layer (dashed lines).

optical property of such artificial dielectric layer is known to depend on the geometrical parameters of the grating and on the effective index of the gap plasmon mode inside the slits and can be approximated by the formula given as reference [147]:

$$\boxed{\bar{n} = \bar{n}_{slit}\frac{d}{f + 2\delta_p}} \tag{4.11}$$

As show in fig.4.7(b) the same optical response is reproduced when we replace an InAsSb grating layer (solid lines) surrounded by air of $d = 2\mu m$, $h = 0.32\mu m$, and $f = 10nm$, with a dielectric layer (dashed lines) of effective thickness $\bar{t} = 23nm$ and $\bar{n} = 55$. It is worth noting that the grating layer does not absorb light since at $\lambda_r = 77\mu m$ approximately 90% of the light is reflected while the rest is transmitted through the slits to the other side of the grating fig.4.7(b). We can see it clearly that for very narrow slits, we will obtain a dielectric layer of very high effective index. The resonant wavelength of the gap plasmon mode is equivalently linked to the effective index and thickness by $\lambda_s = 2\bar{n}\bar{t}$. With these definitions, the whole 1D absorber can be replaced by a much simpler equivalent system made of a dielectric spacer sandwiched between a back mirror assumed to be a perfect

electric conductor (PEC) and an absorbing layer of complex index $\bar{n}$ which mimics the grating layer, Fig. 4.8.

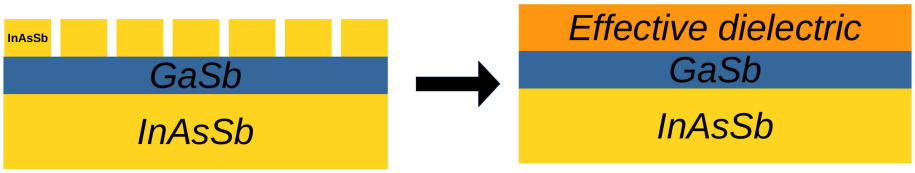

Figure 4.8: Homogenization of the grating layer by an effective dielectric layer with effective index $\bar{n}$ and effective thickness $\bar{t}$.

4.3.2 Second homogenization: All the structure to a single layer

From this three-layered structure, we search for analytical expressions to illustrate the resonant conditions of the FP cavity. By taking into account the PEC back mirror, the magnetic field inside the spacer reads $H_z = Bcos(k_0 n_d y)$, with $k_0 = 2\pi/\lambda$. The electromagnetic continuity conditions applied at the interfaces lead to link by a $\mathbf{T}$ matrix the amplitude B of the spacer mode to the amplitudes I and R of the incident and reflected waves:

$$\begin{pmatrix} I \\ R \end{pmatrix} = \begin{pmatrix} H_y \\ \frac{i}{n_d^2}\frac{\partial H_y}{\partial z} \end{pmatrix} = \mathbf{T} \begin{pmatrix} Bcos(k_0 n_d g) \\ B\frac{k_0}{in_d} sin(k_0 n_d g) \end{pmatrix} \tag{4.12}$$

where $\mathbf{T}$ is a combination of propagation and interface matrices:

$$\mathbf{T} = \frac{1}{2\tau_{01}} \begin{pmatrix} e^{-2ik_0\bar{n}\bar{t}} & \rho e^{2ik_0\bar{n}\bar{t}} \\ \rho e^{-2ik_0\bar{n}\bar{t}} & e^{2ik_0\bar{n}\bar{t}} \end{pmatrix} \begin{pmatrix} 1 & \frac{\bar{n}}{k_0} \\ 1 & -\frac{\bar{n}}{k_0} \end{pmatrix} \tag{4.13}$$

$$\mathbf{T} = \frac{1}{2\tau_{01}} \begin{pmatrix} e^{-2ik_0\bar{n}\bar{t}} + \rho e^{2ik_0\bar{n}\bar{t}} & \frac{\bar{n}}{k_0}(e^{-2ik_0\bar{n}\bar{t}} - \rho e^{2ik_0\bar{n}\bar{t}}) \\ \rho e^{-2ik_0\bar{n}\bar{t}} + e^{2ik_0\bar{n}\bar{t}} & \frac{\bar{n}}{k_0}(\rho e^{-2ik_0\bar{n}\bar{t}} - e^{2ik_0\bar{n}\bar{t}}) \end{pmatrix} = \begin{pmatrix} t_{1,1} & t_{1,2} \\ t_{2,1} & t_{2,2} \end{pmatrix} \tag{4.14}$$

where $\rho = (\bar{n}-1)/(\bar{n}+1)$ is the Fresnel reflection coefficient, and $\tau_{01} = 2\bar{n}/(1+\bar{n})$ is the transmission coefficient. So when substituting eq.(4.14) in eq(4.12) we can express the amplitude of the FP mode in a conventional formulation:

$$B = \frac{2\tau_{eq}}{1 - \Gamma_{eq} e^{2ik_0 n_d g}} I \tag{4.15}$$

Here $\Gamma_{eq} = (1 - \bar{n}_{eq})/(1 + \bar{n}_{eq})$ is an equivalent reflection Fresnel coefficient determined by the equivalent index $\bar{n}_{eq} = \frac{n_d}{k_0}\frac{t_{1,1}}{t_{1,2}}$ related to the elements $t_{i,j}$ of the T-matrix and $\tau_{eq} = t_{1,1} + \frac{k_0}{n_d}t_{1,2}$. Now we can say that our grating and the dielectric layer can be replaced by one single layer of refractive index n_{eq} Fig 4.9. Taking into consideration that n_{eq} simply reduces to n_d when

Figure 4.9: The second homogenization we use, it is replacing the effective dielectric and the spacer GaSb with an equivalent layer of refractive index n_{eq}

the grating is removed leading for eq.(4.15) to the case of a single dielectric slab on top of a PEC mirror (explained in the first section). The analytical expressions for $t_{1,2}$ and $t_{1,1}$ allows to write the equivalent index as

$$\bar{n}_{eq} = \frac{n_d}{\bar{n}} f(\lambda) \tag{4.16}$$

where

$$f(\lambda) = \frac{1 + \rho e^{2i\pi\lambda_s/\lambda}}{1 - \rho e^{2i\pi\lambda_s/\lambda}} \tag{4.17}$$

For thin slits ($d \gg f$) $\rho \simeq 1$ since $\bar{n}$ takes very high values. Thus, in the long wavelength limit, when $\lambda \gg \lambda_s$, the function $f(\lambda)$ can be approximated by $i\lambda/(\pi\lambda_s)$. These simplifications leads to write the equivalent index in the following form:

$$\boxed{\bar{n}_{eq} = \frac{n_d}{n}\frac{\lambda}{\pi\lambda_s}(\frac{\kappa}{n} + i) = n_{eq} + i\kappa_{eq}} \tag{4.18}$$

The good agreement between the exact expression of the complex equivalent index of eq.(4.16) and that of the analytical one of eq.(4.18) is shown in fig.4.10(a). Equipped with this complex equivalent index, the electromagnetic field inside the equivalent layer is enhanced when the denominator of eq.(4.15) is vanished:

$$1 - \Gamma_{eq} e^{2ik_0 n_d g} = 0 \tag{4.19}$$

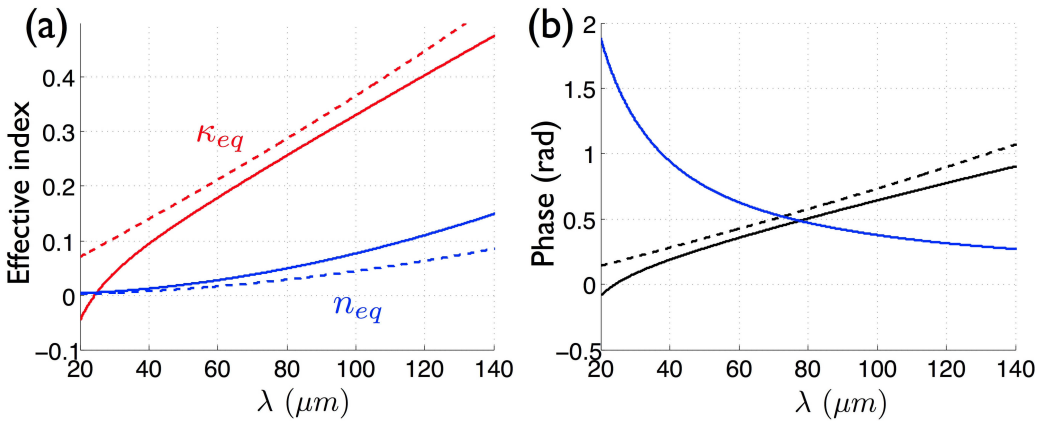

Figure 4.10: (a) Equivalent refractive index and extinction coefficient as a function of the wavelength obtained with Eq.(4.16) in solid curves and with the approximate formulation Eq.(4.18). (b) Phase terms Eq.(4.21): spacer phase $2k_d g$ (blue curve), $-\arg(\Gamma_{eq})$ (black curve) and $2\kappa_{eq}$ (dashed curve).

Two optical conditions (one for phase and a second for the modulus) can be extracted from the magnetic FP resonance eq.(4.19). The first condition, $|\Gamma_{eq}| = 1$, is satisfied for the trivial solution $n_{eq} = 0$ whatever the value of the equivalent absorption κ_{eq}. In practice, almost perfect absorption higher than 98% is achieved when a near-zero equivalent index condition is satisfied, which is the case when $n_{eq} = 0.1$ for instance, see Fig.4.10(a). So from the definition of n_{eq}, we can directly derive an analytical expression for the resonant wavelength:

$$\boxed{\lambda_r = n_{eq}\lambda_s \pi \frac{\mathcal{F}}{n_d} n_{slit} \frac{d}{(f + 2\delta_p)}} \tag{4.20}$$

where $\mathcal{F} = \kappa_{eq}/n_{eq} = n/\kappa$ is the figure of merit (FOM) which is the ratio between the real and the imaginary parts of the equivalent index.

It is worth noting that the shift in the resonant wavelength to larger values is due to the gap plasmon mode inside the slits. The decrease in the width of the slit induces a very high effective index which result in a an extreme slowing down of light with respect to the incident light as illustrated in eq.(4.20) and shown in fig.(4.11).

The second condition is the phase condition which implies that the FP mode is built up inside the spacer and the total phase is cancelled out, so we

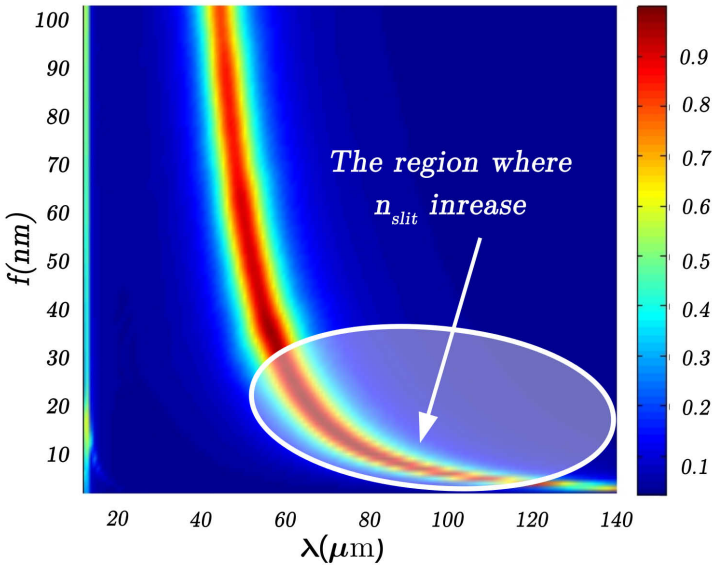

Figure 4.11: Absorbance with respect to the width of the slits f

can write:

$$\arg(\Gamma_{eq}) + 2k_d g = 0 \ [2\pi] \tag{4.21}$$

The first term of Eq.(4.21) can be approximated as following:

$$\Gamma_{eq} = \frac{1 - \bar{n}_{eq}}{1 + \bar{n}_{eq}} = \frac{1 - n_{eq}^2 + \kappa_{eq}^2 - 2i\kappa_{eq}}{(1 + n_{eq})^2 + \kappa_{eq}^2} \tag{4.22}$$

Then $\arg(\Gamma_{eq})$ can be written in this formula:

$$\arg(\Gamma_{eq}) = \frac{-2\kappa_{eq}}{1 - n_{eq}^2 + \kappa_{eq}^2} = \frac{-2\kappa_{eq}}{1 + \kappa_{eq}^2} \tag{4.23}$$

As seen on Fig.(4.10) b, it is well approximated by $\arg(\Gamma_{eq}) = -2\kappa_{eq}$ when the near-zero equivalent index condition is satisfied. So eq.(4.21) can be written as:

$$-2\kappa_{eq} + 2k_d g = 0 \tag{4.24}$$

So that we arrive to the ratio of the spacer's thickness over the wavelength which is given by the following equation:

$$\boxed{\eta = \frac{g}{\lambda_r} = n_{eq} \frac{\mathcal{F}}{2\pi n_d}} \tag{4.25}$$

4.3.3 Asymptotic formulation of the figure of merit FOM

Hence, eq.(4.25) shows that the resonant phase condition is driven by the figure of merit $\mathcal{F}$, which is related to the properties of the gap plasmon mode into the slits:

$$\mathcal{F} = \frac{n}{\kappa} = \frac{n_{slit}}{\kappa_{slit}} \tag{4.26}$$

One could claim that $\mathcal{F}$ thus depends on the choice of the metal utilized for the grating layer. However, we have found that in the quasi-static limit (i.e long wavelength limit) $\mathcal{F}$ can be approximated to a constant $\mathcal{F}_\infty = 8/\pi$ that is independent from the metal choice. So we consider a generalized Drude model for the relative permittivity of the metallic layers that be noble metals or highly doped semiconductors:

$$\varepsilon_r = \varepsilon_\infty - \frac{\omega_p^2}{\omega^2 + i\gamma\omega} \tag{4.27}$$

In the long wavelength limit $\omega/\gamma \ll 1$ so the complex permittivity reads:

$$\varepsilon_r = \varepsilon_\infty - \frac{\omega_p^2}{\gamma^2} + i\frac{\omega_p^2}{\gamma\omega} \tag{4.28}$$

In the case of noble metals $\epsilon_\infty = 1$ and takes values about 10 for semiconductors. Hence (4.28) is well approximated by:

$$\varepsilon_r = \frac{\omega_p^2}{\gamma\omega}(-\frac{\omega}{\gamma} + i) \tag{4.29}$$

Recall that for nanometer slits:

$$\bar{n}_{slit} = \sqrt{\frac{\lambda}{\pi f\sqrt{-\varepsilon_r}}}[94,\ 144] \tag{4.30}$$

By using eq.(4.29), and replacing it in eq.(4.30) we get:

$$\bar{n}_{slit} = \sqrt{\frac{\lambda}{\pi f}}\left(\frac{\gamma\omega}{\omega_p^2}\right)^{1/4}\left(1 - i\frac{\omega}{4\gamma}\right)e^{i\pi/8} \tag{4.31}$$

Then the complex index is written as:

$$\bar{n}_{slit} = \sqrt{\frac{\lambda}{\pi f}}\left(\frac{\gamma\omega}{\omega_p^2}\right)^{1/4}\left|1 - i\frac{\omega}{4\gamma}\right|e^{i\theta_s} \tag{4.32}$$

where $\theta_s \simeq \pi/8 - \omega/(4\gamma)$. The FOM is thus given by $\mathcal{F} = 1/\tan\theta_s$ which is well approximated by:

$$\boxed{\mathcal{F} = \frac{8}{\pi}\left(1 + \frac{2\omega}{\pi\gamma}\right)} \tag{4.33}$$

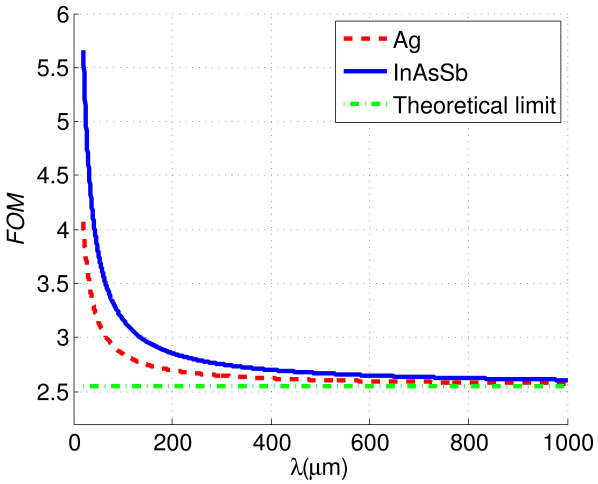

Figure 4.12: Figure of merit with respect to the wavelength for a highly doped semiconductor (InAsSb in solid curve), a noble metal (Ag in dashed curve). The green dot curve shows the quasi-static limit $\mathcal{F}_\infty$.

In the quasi-static limit, $\omega \to 0$, we finally get $\mathcal{F}_\infty = 8/\pi$ or $\mathcal{F}_\infty = 2.54$. Figure 4.12 represents the FOM with respect to the wavelength for InAsSb and for silver [153]. It is seen that these FOMs reach $\mathcal{F}_\infty$ at large wavelengths. These results demonstrate that the FOM and thus that the phase condition for the universal absorbers holds independently from the choice of the metal.

From the asymptotic relation of the figure of merit we arrive to $\eta = 1.1/100$, demonstrating that the FP resonance is better excited when the dielectric layer playing the role of a cavity has a thickness that is roughly only one hundredth of a wavelength. Inserting the equations (4.25) and (4.33) to eq.(4.20), and for nanometer slits ($2\delta \gg f$), we get a simple expression for the resonant wavelength of the FP mode:

$$\boxed{\lambda_r = \Lambda\frac{d}{\sqrt{f}}} \tag{4.34}$$

with $\Lambda = 2\eta\pi^2\lambda_s/\sqrt{2\delta_p}$ that can be evaluated for 10-nanometer slits to $\Lambda = 3.38$. Finally, Eq.(4.25) and Eq.(4.34) provide simple scaling laws for designing universal absorbers operating at arbitrary large wavelengths.

4.3.4 Total absorption due to a negative phase

The previous derived scaling laws shows that our absorber is universal in the sense that its absorption mechanism does not depend on the metal choice and consequently is not affected by the metal dispersion. So in order to get an absorbance higher than 95% we have to set $n_{eq} = 0.1$ with this parameter we arrive to $\eta = 1.1/100$, which demonstrate that the FP resonance is better excited when the dielectric spacer play the role of a cavity of a thickness that is roughly one hundredth of the operating wavelength. This property

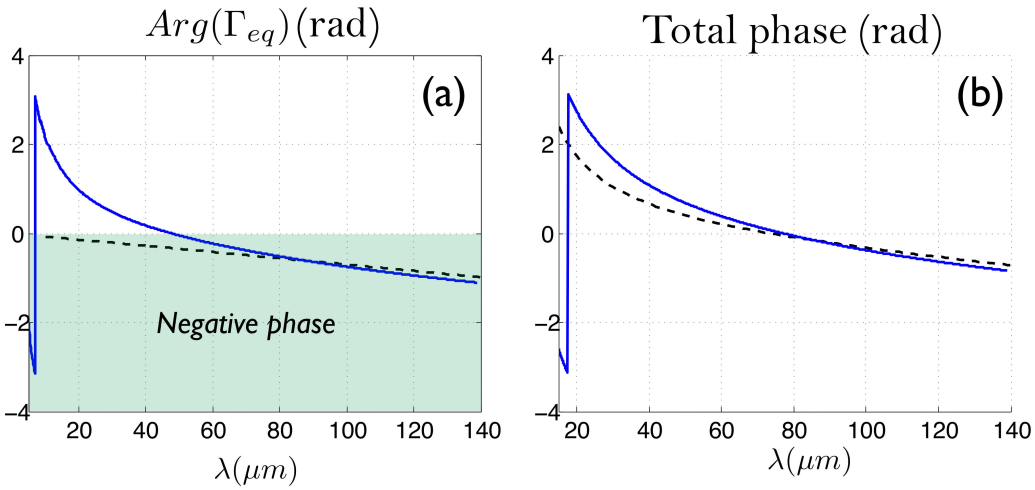

Figure 4.13: (a) Phase of the equivalent Frensel coefficient. The solid and dashed curves are respectively $\arg(\Gamma_{RCWA})$ and $-2\kappa_{eq}$.(b) Total phase through the metamaterial. The solid and dashed curves are respectively Φ_{RCWA} and Φ_{eq}.

originates from the negative phase, $-2\kappa_{eq}$, acquired by the electromagnetic waves when they are reflected by the equivalent high index dielectric layer. We compare the phase of the equivalent Fresnel coefficient $arg(\Gamma_{eq})$ derived from the equivalent dielectric model and that from the exact reflection coefficient extracted from the RCWA code. This phase was found to be negative

around the absorption line and reach an asymptotic function $-2\kappa_{eq}$ Fig.4.16 (a). This is confirmed by RCWA method which relies on the computation of the scattering matrices of sub-structures of the device. These scattering matrices explicitly contain the reflection and transmission coefficient related to any given sub-structure. It thus gives access to the reflection coefficient of a plane wave propagating inside the spacer in normal incidence on the metamaterial layer r_{MM}, and on the back mirror r_{Mirror}. we have then:

$$\arg(\Gamma_{RCWA}) = \arg(r_{MM}) + \arg(r_{Mirror}) \tag{4.35}$$

We derive the analytical expression of the total phase that cancels at the FP resonance Fig.4.16(b):

$$\Phi_{eq} = -2\kappa_{eq} + 2k_d g \tag{4.36}$$

and the exact total phase calculated from the RCWA method:

$$\Phi_{RCWA} = \arg(\Gamma_{RCWA}) + 2k_d g \tag{4.37}$$

where $k_d = 2\pi/\lambda n_d$. These results demonstrate that the metamaterial interface introduces a negative phase shift responsible for the near-zero thickness of the dielectric spacer.

4.4 Perfect absorbers from infrared to microwave

In order to confirm our scaling results, we draw in figure (4.14a) the resonant wavelength as a function of the grating periods d ranging from 1 μm to 400 μm. This result is in agreement with our model, since the resonant wavelength is seen to be linearly linked to the period by $\lambda_r \simeq 33d$ (for d in microns). The use of Eq.(4.34) for slits of 10 nm wide leads to a slope of 33.8, thus confirming the excellent accuracy of our analytical model. This means that the structure is able to absorb microwaves with a wavelength that is more than 6 orders of magnitude larger than the slits' width. The electric field associated to this FP magnetic resonance is actually squeezed in slits that are a million times smaller than the wavelength. This is where the absorption takes place, since the dielectric spacer is considered lossless. As seen on Fig. 4.14(b), the dimension of the slits have an important impact on the spectral position of the magnetic FP resonance. This is especially

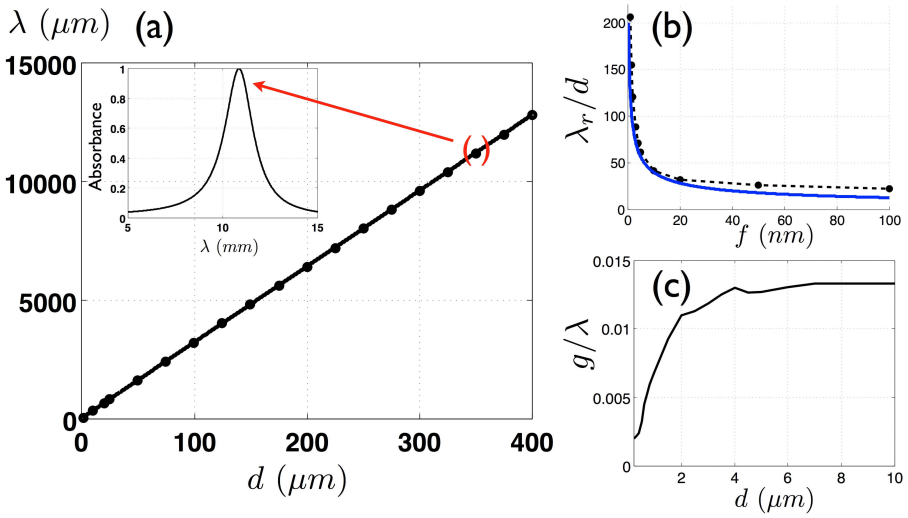

Figure 4.14: (a) Resonant wavelength λ_r as a function to the pitch d for a 1D absorber. The bold line corresponds to the theoretical scaling law $\lambda_r = 33d$ and the dots to the exact electromagnetic computations. The inset represents the absorbance spectrum with a total absorption in the microwave range for $\lambda_r = 11.2\ mm$ when $d = 350\ \mu m$. (b) Ratio λ_r/d with respect to the slit width, the dashed and solid curves are respectively obtained with the RCWA simulations and with Eq.(4.34) for $d = 1\ \mu m$. (c) Ratio of the spacer over the wavelength with respect to the pitch. g/λ remains constant for a period larger than 8 μm.

true when they are a few nanometers wide, as this dimension has a very large influence on the effective index of the gap-plasmon propagating in the slits. A quite good agreement is observed with the exact results obtained using the RCWA simulations and Eq.(4.34) for $d = 1\ \mu m$. Beyond a pitch of 4 μm or equivalently for wavelengths larger than 100 μm, the thickness of the spacer remains constant about $g/\lambda = 1.3/100$, close to the theoretical limit $\eta = 1.1/100$, Fig. 4.14 (c). For arbitrarily large wavelengths, the slits operate as antennas that funnel the incident waves into the spacer that constitutes the resonant cavity. The funneling factor, the ratio of the pitch to the slid width, is huge: it can be as large as 40,000 which is way above what usually happens for EOT when the resonance is located in the slits. This mechanism holds from the infrared to the microwave range despite the dispersive behaviour of InAsSb and can be obtained for other metals such as

silver.

4.5 2D perfect absorbers and insensitivity to the polarization

From the application point of view, realizing absorbers insensitive to the incident angle and to the polarization of light is a crucial issue. We address these problems by considering 2D metamaterial absorbers made of a square array of thin slits (width $f = 10\ nm$) separated by a pitch $d = 2\mu m$, Fig. 4.15(a). We illustrate these properties for a targeted absorption line at $\lambda_r = 70\mu m$ leading to a spacer's thickness $g = 850\ nm$, a pitch $d = 2\ \mu m$ and a grating's thickness $h_r = 320\ nm$. More than 90% of the incident radiation is absorbed by the metamaterial for incident angles up to 50° and the absorbance reaches 70% at grazing incidence for 70°, Fig. 4.15(b-c). The efficiency of the absorber is also seen to be insensitive to the polarization of light: the structure can simply be seen as two crossed gratings, each one being responsive to one polarization only. In normal incidence, the absorbance thus remains constant whatever the polarization in normal incidence.

4.6 Universal absorber made of silver

Since our design is universal and can efficiently operate regardless the metal used. We demonstrate this property considering silver for the metallic layers. We consider a spacer with a refractive index $n_d = 3.7$, slits of width $f = 10\ nm$ etched in a grating whose thickness is $h = 20\ nm$. The slits support a gap plasmon resonance for $\lambda_s = 1\ \mu m$ which leads to a constant $\Lambda = 1.24$ (for a skin depth $\delta_p = 25\ nm$). The equivalent dielectric model leads to $g/\lambda_r = 1.1/100$ and $\lambda_r = 12.4d$ (for the pitch d expressed in microns). These results are confirmed by the direct computation of the absorption line corresponding to the magnetic FP resonance for different lattice periods, Fig. 4.16(a). We found a linear variation $\lambda_r = 14.2d$ in agreement with the theoretical prediction (with an error of 13%). The actual relative thickness of the spacer converges to 1.4/100, a value very close to the theoretical one, Fig. 4.16(b).

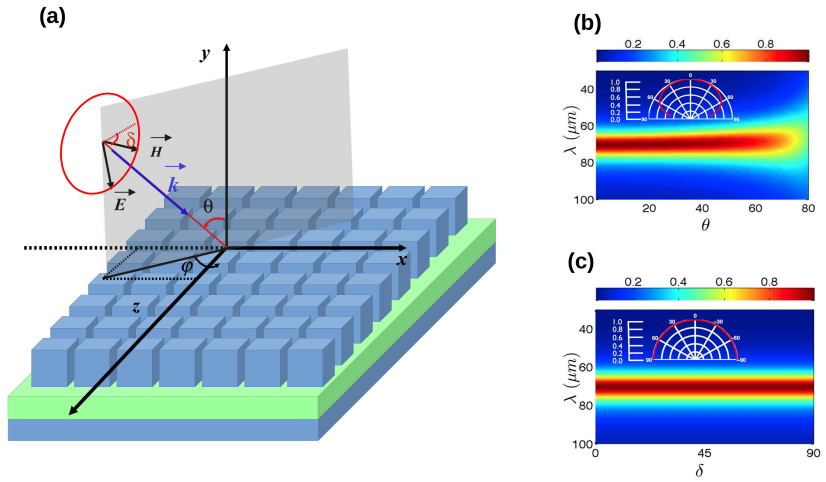

Figure 4.15: (a) Schematic representation of the 2D universal absorber. (b) Absorbance with respect to the incident angle θ and for a polarization angle $\delta = 0°$. The inset represents the polar plot of the absorbance computed for the absorption line $\lambda_r = 70\mu m$. (c) Absorbance with respect to the polarization angle δ and for the normal incidence (TM and TE polarizations cases are respectively defined by $\delta = 0°$ and $\delta = 90°$. The inset shows the polar plot of the absorption line as a function of δ.

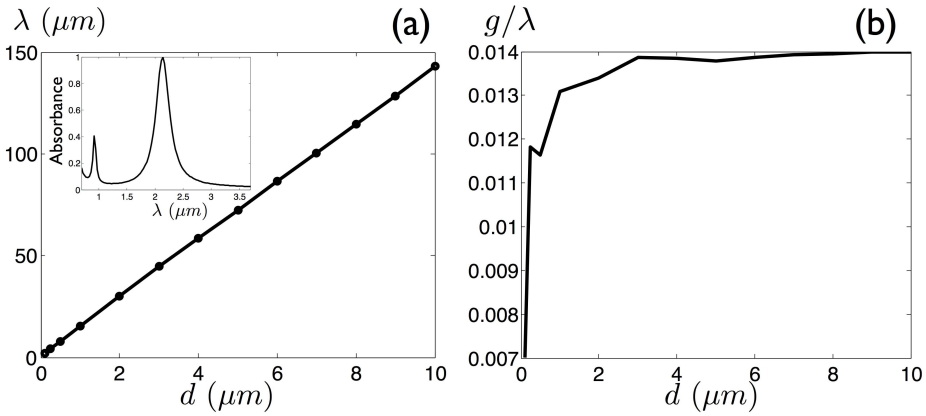

Figure 4.16: (a) Resonant wavelength with respect to the pitch d for a 1D silver universal absorber with slits of width $f = 20nm$. (b) g/λ_r as a function of d.

4.7 Conclusion

We have proposed a metamaterial resonant absorber whose absorption line can be chosen in any frequency range, from optics to microwaves, by following simple scaling laws, essentially. Our approach allows to design a perfect absorber that working for any frequency, independently of the materials that are considered. Almost perfect absorption is reached whatever the polarization and over a broad incident angle range. This is why we think our design can be said to be *universal*. The metamaterial layer controlling the response of the structure allows to reduce to $\lambda/100$ the thickness of the spacing layer constituting a resonant cavity on which the device is based. The absorption takes place in slits that are no more than a few nanometers wide, despite wavelengths that are 1,000,000 times larger. All the incoming radiation in funnelled through these slits despite a ratio of 1 to 40,000 between the slit width and the period. We have derived an analytical model thoroughly describing the electromagnetic response of the device that proved very accurate despite these extreme and unprecedented ratios. In comparison to the approaches Kats used our design introduce a huge phase shift the allows the extreme reduction of the size of the dielectric layer as shown in figure (4.17). These Universal absorbers constitute ultra-thin and flexible solutions for absorbing any kind of electromagnetic radiation especially at terahertz frequencies where absorbers, sensors and emitters are usually difficult to design. Integrating electric contacts into the device or making it dynamically tunable is something that can totally be envisaged, broadening even more the potential of our design.

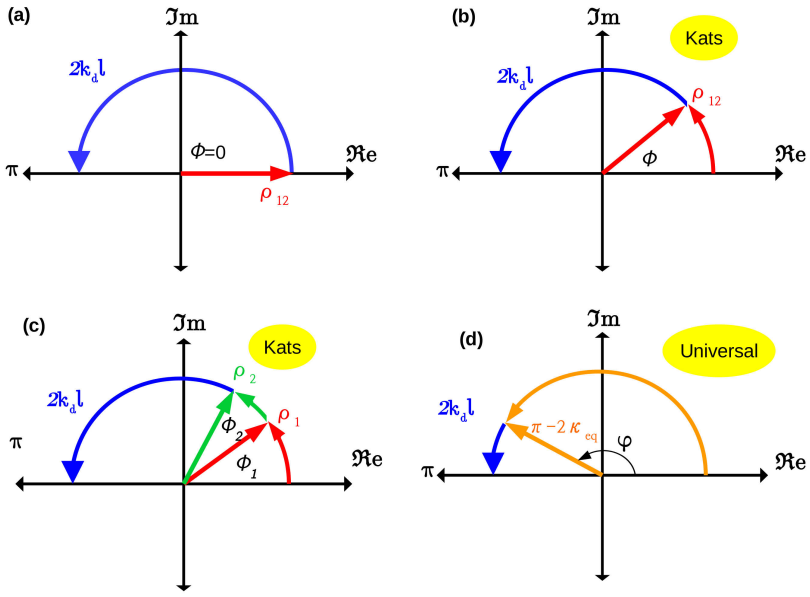

Figure 4.17: (a) Phasor diagrams of a zero or a very small imaginary part of the dielectric medium backed with a PEC mirror. (b) Is for a dielectric layer with losses and a PEC mirror. (c) For a lossy dielectric layer backed with a layer of finite conductivity.(d) Is the universal approach of an effective dielectric layer with a huge phase shift.

General conclusion

In this thesis, we showed the first demonstration of InAsSb:Si MIM resonators in the far-infrared range. The theoretical study is confirmed by the experimental results, that shows a very good agreement. This verify that highly doped semiconductors are promising candidates for realizing plasmonic structures in the THz region. In addition to their tunable optical properties HDSC, are compatible with CMOS technology and cheap adding an interesting advantage that can open new avenues in commercializing plasmonics and benefit from them in real life such as biological sensorsand cancer treatment.

We then demonstrate that MIM antennas can be miniaturized by a factor of 100 compared to classical MIM structures just by replacing the dielectric layer by hyperbolic metamaterial medium. This technique adds a degree of freedom to the plasmonic system that enable further manipulation of light is subwavelength scales. These approach can be used in either in metals or highly doped semiconductors so they can operate in different frequency ranges. In addition to their integrated sizes hyperbolic wires overcome the limitations of standard plasmonic resonators.

Finally, a universal metamaterial absorber is proposed, the unique properties of this design is the material barrier that always imposes the spectral domain of operation had been overcame. Instead, geometrical parameters are responsible for the resonant wavelengths. This absorber can be used in the field of electrically tunable metamaterials, where the carrier density of semiconductors can be controlled by an external bias voltage leading to a manipulation of light in the real time [154].

We believe that our work in this thesis might have a good impact in the field of plasmonics and can benefit real life applications (i.e MIM). On the other hand, the theoretical study of hyperbolic wires and the universal absorbers will pave the way for realizing extraordinary and integrated

structures. The challenges now are now in finding the suitable fabrication techniques for their realization.

Bibliography

[1] R. H. Ritchie,"Plasma losses by fast electrons in thin films ", Physical Review **106:874**, (1957).

[2] N. W. Ashcroft and N. D. Mermin, Solid State Physics, 1. ed. (Harcourt College Publisher, Philadelphia), $1 - 20$, (1976).

[3] C. L. C. Smith, N. Stenger, A. Kristensen, N. A. Mortensen, and S. I. Bozhevolnyi, " Gap and channeled plasmons in tapered grooves: a review", Nanoscale **7**, 9355, (2015)

[4] S. Bozhevolnyi and T. Sondergaard, " General properties of slow plasmon resonat nanostructures: nano -antennas and resonators," Optics Express, **15**, (2007).

[5] N. Fang, H. Lee, C. Sun, and X. Zhang,"SubDiffraction-Limited Optical Imaging with a Silver Superlens," Science, **308**, 534-537 (2005)

[6] D. O. S. Melville and R. J. Blaikie, "Super-resolution imaging through a planar silver layer, " Optics Express, **13**, 2127-2134 (2005).

[7] Z. Liu, H. Lee, Y. Xiong, C. Sun, and X. Zhang, "Far-field optical hyperlens magnifying sub-diffraction-limited objects, "Science **315**, 1686-1686 (2007)

[8] G. Dolling, M. Wegener, C. M. Soukoulis, and S. Linden,"Negative-index metamaterial at 780nm wavelength " Opt. Lett., **32**, 53-55 (2007).

[9] T. W. Ebbesen, H. J. Lezec, H. F. Ghaemi, T. Thio, and P. A. Wolff, "Extraordinary optical transmission through sub-wavelength hole arrays," Nature **391**, 667-669 (1998).

[10] V. M. Shalaev, W. Cai, U. K. Chettiar, H. K. Yuan, A. K. Sarychev, V. P. Drachev, and A. V. Kildishev,"Negative index of refraction in optical metamaterials ," Opt. Lett. **30**, 3356-3358 (2005).

[11] R. Smaali, F. Omeis, A. Moreau, E. Centeno, and T. Taliercio, "Miniaturizing optical antennas using hyperbolic metamaterial wires," Phys. Rev. B, **95**, 155306 (2017).

[12] K. S. Novoselov, A. K. Geim, S. V. Morozov, D. Jiang, M. I. Katsnelson, I. V. Grigorieva, S. V. Dubonos,and A. A. Firsov, "Two-dimensional gas of massless Dirac fermions in graphene," Nature **438**, 4233, (2005).

[13] O. Vafek, "Thermoplasma polariton within scaling theory of single-layer graphene," Physical review letters, **97**, 266406, (2006).

[14] V. Ryzhii, "Terahertz Plasma Waves in Gated Graphene Heterostructures," Japanese Journal of Applied Physics, **45**, 33-36, (2006).

[15] V. Ryzhii, M. Ryzhii and T. Otsuji, "Tunneling CurrentVoltage Characteristics of Graphene Field-Effect Transistor," Applied Physics Express, **1**, (2007)

[16] L. A. Falkovsky and A. A. Varlamov, "Space-time dispersion of graphene conductivity," Eur. Phys. J. B **56**, 281-284 (2007).

[17] R. M. Woodward, V. P. Wallace, R. J. Pye, B. E. Cole, D. D. Arnone, E.H. Linfield, and M. Pepper,"Terahertz pulse imaging of ex vivo basal cell carcinoma," J. Investigative Dermatol **120**, 72-78, (2003)

[18] A. Markelz, S. Whitmore, J. Hillebrecht, and R. Birge, "THz time domain spectroscopy of bimolecular conformational modes," Phys. Med. Biol., **47**, 3797-3805, (2002).

[19] S. P. Mickan, A. Menikhu, H. Liu, C. A. Mannella, R. MacColl, D. Abbott, J. Munch, and X.-C. Zhang, "Label-free bioaffinity detection using terahertz technology," Phys. Med. Biol., **47**, 3789-3795,(2002).

[20] P. H. Bolivar, M. Brucherseifer, M. Nagel, H. Kurz, A. Bosserhoff, and R. Buttner, Label-free probing of genes by time domain terahertz sensing," Phys. Med. Biol., **47**, 3815-3821, (2002).

[21] K. J. Seibert, T. Loffler, H. Quast, M. Thomson, T. Bauer, R. Leonhardt, S. Czasch, and H. G. Roskos, "All-optoelectronic continuous wave THz imaging for biomedical applications," Phys. Med. Biol., **47**, 3743-3748, (2002).

[22] A. J. Fitzgerald, E. Berry, N. N. Zinovev, S. HomerVanniasinkam, R. E. Miles, J. M. Chamberlain, and M. A. Smith, "Catalogue of human tissue optical properties at terahertz frequencies," J. Biol. Phys.,**29**, 123-128, (2003).

[23] M. R. Scarfi, M. Romano, R. Di Pietro, O. Zeni, A. Doria, G. P. Gallerano, E. Giovenale, G. Messina, A. Lai, G. Campurra, D. Coniglio, and M. DArienzo, "THz exposure of whole blood for the study of biological effects on human lymphocytes," J. Biol. Phys.,**29**, 171-176, (2003)

[24] R. F. Oulton et al. " Plasmon lasers at deep subwavelength scale." Nature,**461**, 629-632, (2009)

[25] M. Hill et al., "Lasing in metal-insulator-metal sub-wavelength plasmonic waveguides," Opt. Express **17**, 11107-11114 (2009)

[26] T. G. Phillips and J. Keene, "Submillimeter astronomy," Proc. IEEE, **80**, 1662-1678, (1992)

[27] Pendry JB, "Negative refraction makes a perfect lens," Phys. Rev. Lett. **85**, 3966-3969, (2000).

[28] Z. Jacob, L. V. Alekseyev, E. Narimanov, "Optical hyperlens: far-field imaging beyond the diffraction limit," Opt. Express, **14**, 8247-8247 (2006)

[29] D. Schurig, JJ. Mock, BJ. Justice, SA. Cummer, JB. Pendry, AF. Starr, DR. Smith, "Metamaterial electromagnetic cloak at microwave frequencies," Science, **314**, 977-980 (2006).

[30] A. Kabashin, P. Evans, S. Pastkovsky, W. Hendren, G. Wurtz, R. Atkinson, R. Pollard, V. Podolskiy, A. Zayats, "Plasmonic nanorod metamaterials for biosensing," Nat. Mater. **8**, 867-871, (2009).

[31] AA. Govyadinov, VA. Podolskiy, "Metamaterial photonic funnels for subdiffraction light compression and propagation," Phys. Rev. B,**73**, (2006).

[32] II Smolyaninov, Y-J. Hung, "Modeling of time with metamaterials," J. Opt. Soc. Am. B, **28**, 1591-1595 (2011).

[33] S. Zhang, W. Fan, N. C. Panoiu, K. J. Malloy, R. M. Osgood, and S. R. J. Brueck, "Experimental Demonstration of Near-Infrared Negative-Index Metamaterials," Physical Review Letters," **95**, (2005).

[34] X. Zhang, M. Davanco, Y. Urzhumov, G. Shvets, and S. R. Forrest, "From Scattering Parameters to Snells Law: A Subwavelength Near-Infrared Negative-Index Metamaterial," Physical Review Letters, **101**, (2008)

[35] K. Konstantinidis and A. P. Feresidis,"Broadband near-zero index metamaterials," J. Opt. **17** (2015)

[36] P. Shekhar, J. Atkinson, and Z. Jacob, "Hyperbolic metamaterials: fundamentals and applications," Nano Convergence **1**, (2014)

[37] D. R. Smith, N. Kroll, "Negative refractive index in left handed materials," Phys. Rev. Lett. **85**, 2933-2936, (2000)

[38] R. Shelby, D. Smith, S. Schultz, " Experimental verification of a negative index of refraction," Science, **292**, 77-79, (2001)

[39] J. Valentine, S. Zhang, T. Zentgraf, E. Ulin-Avila, DA. Genov, G. Bartal, X. Zhang, " Three dimensional optical metamaterial with a negative refractive index," Nature, **455**, 376-379, (2008).

[40] J. A. Dionne, E. Verhagen, A. Polman, and H. A. Atwater, "Are negative index materials achievable with surface plasmon waveguides? A case study of three plasmonic geometries," Optics Exp. **16**, (2008).

[41] Hocheol Shin and Shanhui Fan, "All-Angle Negative Refraction for Surface Plasmon Waves Using a Metal-Dielectric-Metal Structure," Physical Review Letters, **96**, (2006)

[42] E. Verhagen, R. de Waele, L. Kobus Kuipers, and A. Polman, "Three Dimensional Negative Index of Refraction at Optical Frequencies by Coupling Plasmonic Waveguides," Physical Review Letters, **105** (2010)

[43] N. Yu, P. Genevet, M. A. Kats, F. Aieta, J-P. Tetienne, F. Capasso, Z. Gaburro, "Light Propagation with Phase Discontinuities: Generalized Laws of Reflection and Refraction," Science **334** 333337 (2011)

[44] Shulin Sun , Qiong He, Shiyi Xiao, Qin Xu, Xin Li and Lei Zhou, "Gradient-index meta-surfaces as a bridge linking propagating waves and surface waves," Nature materials, **11**, 426-431 (2012)

[45] J.N. Farahani, H.-J. Eisler, D.W. Pohl, M. Pavius, P. Fluckiger, P. Gasser, B. Hecht. "X-shaped plasmonic antenna on a quantum cascade laser ", Nanotechnology **18**, 125506 (2007)

[46] L. Lin, Y. Zheng."Optimizing plasmonic nanoantennas via coordinated multiple coupling", Sci. Rep., **5** 14788 (2015)

[47] M.F.G Klein, H. Jein, P.-J. Jakobs, S. Linden, N. Meinzer, M. Wegener, V. Saile, M. Kohl. "Electron beam lithography of V-shaped silver nanoantennas", Micro. Eng. **86**, 1078 (2009)

[48] A. Saeed, S. Panaro, R. Proietti Zaccaria, W. Raja, C. Liberale, M. Dipalo, G. C. Messina, H. Wang, F. De Angelis and A. Toma, "Stacked optical antennas for plasmon propagation in a 5 nm-confined cavity", Sci. Rep.,**5**, 11237 (2015).

[49] G. M. Akselrod, C. Argyropoulos, T. B. Hoang, C. Ciraci, C. Fang, J. Huang, D. R. Smith, and M. H. Mikkelsen, "Probing the mechanisms of large Purcell enhancement in plasmonic nanoantennas", Nature Photon. **10**, 1038 (2014)

[50] J. Hao, L. Zhou, and M. Qiu, "Nearly total absorption of light and heat generation by plasmonic metamaterials", Phys. Rev. B **83**, 165107 (2011).

[51] Y. Chu, D. Wang, W.Zhu, K.-B. Crozier, "Beamed Raman: directional excitation and emission enhancement in a plasmonic crystal double resonance SERS substrate ", Opt. Exp. **19**(16), 14919 (2011).

[52] A. Cattoni, P. Ghenuche, A-M. Haghiri-Gosnet, D. Decanini, J. Chen, J-L. Pelouard, S. Collin, "$\lambda^3/1000$ plasmonic nanocavities for biosensing fabricated by soft UV nanoimprint lithography", Nano Lett, **11** 3557-3563 (2011)

[53] N. Vandamme, H.-L. Chen, A. Gaucher, B. Behaghel, A. Lemaitre, A. Cattoni, C. Dupuis, N. Bardou, J.-F. Guillemoles, and S. Collin. "Ultrathin GaAs solar cells with a silver back mirror", IEEE Journal of Photovoltaic, **5** 565 (2015).

[54] F. Bigourdan, F. Marquier, J.-P. Hugonin, and J.-J. Greffet, "Design of highly efficient metallo-dielectric patch antennas for single-photon emission", Opt. Exp. **22**(3) 2337 (2014)

[55] H.-H. Chen, H.-H. Hsiao, H.-C. Chang, W.-L. Huang, and S.-C. Lee, "Double wavelength infrared emission by localized surface plasmonic thermal emitter " Appl. Phys. Lett **104** 083114 (2014).

[56] J.-F. Federici, B. Schulkin, F. Huang, D. Gary, R. Barat, F. Oliveira and D. Zimdars, "THz imaging and sensing for security applicationsexplosives, weapons and drugs", Semicond. Sci. Technol **20** S266-S280 (2005)

[57] G. Liang, X. Hu, X. Yu, Y. Shen, L.-H. Li, A. Giles Davies, E.-H. Linfield, H.-K. Liang, Y. Zhang, S.-F. Yu, and Q.-J. Wang, "Integrated terahertz graphene modulator with 100% modulation depth", ACS Photonoic **2** 1559-1566 (2015)

[58] E. Pickwell and V.-P. Wallace,"Biomedical applications of terahertz technology", J. Phys. D: Appl. Phys. **39** R301-R310 (2006)

[59] S. Koenig, D. Lopez-Diaz, J. Antes, F. Boes, R. Henneberger, A. Leuther, A. Tessmann, R. Schmogrow, D. Hillerkuss, R. Palmer, T. Zwick, C. Koos, W. Freude, O. Ambacher, J. Leuthold and I. Kallfass, "Wireless sub-THz communication system with high data rate", Nat. Phot. **10** 1038 (2013)

[60] G. Isić and R. Gajić ,"Geometrical scaling and modal decay rates in periodic arrays of deeply subwavelength Terahertz resonators", J. Appl. Phys **116**, 233103 (2014)

[61] D. Palaferri, Y. Todorov , Y. N. Chen, J. Madeo , A. Vasanelli, L. H. Li, A. G. Davies, E. H. Linfield, and C. Sirtori, "Patch antenna terahertz photodetectors", Appl. Phys. Lett. **106**, 161102 (2015)

[62] H. Hang, Y. Li, Y. Yong-Hong, "Near-field enhancement and absorption properties of metal-dielectric-metal microcavities in the mid-infrared range", Chin. Phys. Lett. **31** 018101 (2014)

[63] M. G. Blaber, M. D. Arnold, M. J. Ford, "Optical properties of intermetallic compounds from first principles calculations: a search for the ideal plasmonic material", J. Phys. Condens. Matter **21** 144211 (2009)

[64] M. G. Blaber, M. D. Arnold, N. Harris, M. J. Ford, and M. B. Cortie, "Plasmon absorption in nanospheres: A comparison of sodium, potassium, aluminium, silver and gold", Physica B **394**, 184187 (2007).

[65] V. N'Tsame Guilengui, L. Cerutti, J.B. Rodriguez, E. Tournie, T. Taliercio, "Localized surface plasmon resonances in highly doped semiconductors nanostructures ", Appl. Phys. Lett. **101** 161113,(2012)

[66] A. J. Hoffman, L. Alekseyev, S. S. Howard, K. J. Franz, D. Wasserman, V. A. Podolskiy, E. E. Narimanov, D. L. Sivco, and C. Gmachl, "Negative refraction in semiconductor metamaterials", Nat. Mater. **6**, 946-950 (2007)

[67] J. C. Ginn, R. L. Jarecki Jr., E. A. Shaner, and P. S. Davids, "Infrared surface plasmons on heavily doped silicon", J. Appl. Phys. **110**, 043110 (2011)

[68] M. Fehrenbacher, S. Winnerl, H. Schneider, J. Doring, S. C. Kehr, L. M. Eng, Y. Huo, O. G. Schmidt, K. Yao, Y. Liu, and M. Helm, "Plasmonic superlensing in doped GaAs", Nano Lett. **15**, 1057-1061 (2015)

[69] J. Frigerio, A. Ballabio, G. Isella, E. Sakat, G. Pellegrini, P. Biagioni, M. Bollani, E. Napolitani, C. Manganelli, M. Virgilio, A. Grupp, M. P. Fischer, D. Brida, K. Gallacher, D. J. Paul, L. Baldassarre, P. Calvani, V. Giliberti, A. Nucara, and M. Ortolani, "Tunability of the dielectric function of heavily doped germanium thin films for mid-infrared plasmonics", Phys. Rev. B **94**, 085202 (2016)

[70] S. Law, D.C. Adams, A.M. Taylor, D. Wasserman, "Mid-infrared designer metals", Opt. Express **20**, 12155-12165 (2012)

[71] F. Barho , F. Gonzalez-Posada, M.-J. Milla-Rodrigo, M. Bomers, L. Cerutti, and T. Taliercio, "All-semiconductor plasmonic gratings for

biosensing applications in the mid-infrared spectral range", Opt. Express **24**(14) 16176 (2016)

[72] S. Roux, P. Barritault, O. Lartigue, L. Cerutti, E. Tournie, B. Grard, and A. Grisard, Appl. Phys. Lett. **107**, 171901 (2015)

[73] Bharadwaj P.; Deutsch B.; Novotny L. "Optical antennas" Advances in Optics and Photonics **1**, 438-483 (2009).

[74] A. Shaltout, J. Liu, A. Kildishev, and V. Shalaev,"Photonic spin Hall effect in gap plasmon metasurfaces for on-chip chiroptical spectroscopy."Optica, **8**, 860 (2015)

[75] Huang K. C. Y., Seo M.-K., Sarmiento T., Huo Y., Harris J.S. , Brongersma M. L.,"Electrically driven subwavelength optical nanocircuits." Nature Photonics, **8**,244 (2014)

[76] West P.; Ishii S.; Naik G.; Emani N.; Shalaev V.; Boltasseva A. "Searching for better plasmonic materials", Laser and Photonic Reviews, **4**, 795-808 (2010)

[77] Tokumitsu E. "Correlation between Fermi level stabilization positions and maximum free carrier concentrations in III-V compound semiconductors". Japanease journal for applied physics, **29**, L698-L701 (1990)

[78] Taliercio T.; Ntsame Guilengui V.; Cerutti L.; Rodriguez J.-B.; Tourni E. "GaSb- based all-semiconductor mid-IR plasmonics", Proc. SPIE, 8631, 86318672 (2013)

[79] Vurgaftman I.; Meyer J. R.; Ram-Mohan L. R. " Band Parameters for III-V compound semiconductors and their alloys", J. Applied Physics, **89**(11), 5815 (2001)

[80] Weiss, T., Granet, G., Gippius, N. A., Tikhodeev, S. G. "Matched coordinates and adaptive spatial resolution in the Fourier modal method" Opt. Express **17**, 8051–8061 (2009).

[81] Mikhailova M. P.; in Handbook series on semiconductor parameters, Levinshtein M.; Rumyantsev S.; Shur M., ed. *World scientific*, **1**, 147-168 (1996)

[82] Kekatpure R. D.; Hryciw A.C.; Bernard E. S.; Brongersma M. L., "Solving dielectric and plasmonic waveguide dispersion relations on a pocket calculator", Opt. Express , **17**, 24112-24129 (2009)

[83] T. Xu, Y. K. Wu, X. Luo, and L. J. Guo,"Plasmonic nanoresonators for high-resolution colour fi ltering and spectral imaging," Nature Commun. **1**, 1-5 (2010)

[84] N. Liu, M. Mesch, T. Weiss, M. Hentschel, and H. Giessen, "Infrared Perfect Absorber and Its Application As Plasmonic Sensor,"**10**, 2342-2348 (2010)

[85] P. Bharadwaj, B. Deutsch, and L. Novotny, "Optical Antennas", Adv. Opt. Photon. **1**, 438 (2009).

[86] A. Shaltout, J. Liu, A. Kildishev, and V. Shalaev,"Photonic spin Hall effect in gapplasmon metasurfaces for on-chip chiroptical spectroscopy", Optica **2**, 860 (2015).

[87] K. C. Y. Huang, M.-K. Seo, T. Sarmiento, Y. Huo, J. S. Harris, and M. L. Brongersma, "Electrically driven subwavelength optical nanocircuits", Nat Photonics **8**, 244 (2014).

[88] A. Pors, O. Albrektsen, I. P. Radko, and S. I. Bozhevolnyi, "Gap plasmon-based metasurfaces for total control of reflected light", Scientific Reports **3**, 2155 (2013).

[89] R. Esteban, T. V. Teperik, and J. J. Greffet, "Optical Patch Antennas for Single Photon Emission Using Surface Plasmon Resonances",Phys Rev Lett, **104**, 026802 (2010).

[90] R. Smaali, F. Omeis, A. Moreau, T. Taliercio, and E. Centeno, "A universal design to realize a tunable perfect absorber from infrared to microwaves", Scientific Reports **6**, 32589 (2016).

[91] M. Miyata, A. Holsteen, Y. Nagasaki, M. L. Brongersma, and J. Takahara, "Gap Plasmon Resonance in a Suspended Plasmonic Nanowire Coupled to a Metallic Substrate", Nano Lett. **15**, 5609 (2015).

[92] C. Tserkezis, R. Esteban, D. O. Sigle, J. Mertens, L. O. Herrmann, J. J. Baumberg, and J. Aizpurua, "Hybridization of plasmonic antenna

and cavity modes: Extreme optics of nanoparticle-on-mirror nanogaps", Phys. Rev. A **92**, 053811(2015).

[93] I. Puscasu, W. L. Schaich, " Narrow-band, tunable infrared emission from arrays of microstrip patches", Appl. Phys. Lett., **92**, 233102 (2008).

[94] F. Pardo, P. Bouchon, R. Haidar, J.L. Pelouard, "Light Funneling Mechanism Explained by Magnetoelectric Interference", Phys. Rev. Lett. **107**, 093902 (2011).

[95] G. M. Akselrod, J. Huang, T. B. Hoang, P. T. Bowen, L. Su, D. R. Smith, and M. H. Mikkelsen,"Large-Area Metasurface Perfect Absorbers from Visible to Near-Infrared", Adv. Mater. **27**, 8028 (2015).

[96] A. Moreau, C. Ciraci, J. J. Mock, R. T. Hill, Q. Wang, and B. J. Wiley, "Controlled-reflectance surfaces with film-coupled colloidal nanoantennas", Nature **492**, 86 (2012).

[97] R. Chikkaraddy, B. de Nijs, F. Benz, S. J. Barrow, O. A. Scherman, E. Rosta, A. Demetriadou, P. Fox, O. Hess, and J. J. Baumberg, "Single-molecule strong coupling at room temperature in plasmonic nanocavities", Nature **535**, 127 (2016).

[98] F. Bigourdan, F. Marquier, J. P. Hugonin, and J. J. Greffet, "Design of highly efficient metallo-dielectric patch antennas for single-photon emission ", Opt. Expr. **22**, 2337 (2014).

[99] A. Lefebvre, D. Costantini, I. Doyen, Q. Lvesque, E. Lorent, D. Jacolin, J. J. Greffet, S. Boutami, and H. Benisty, "CMOS compatible metal-insulator-metal plasmonic perfect absorbers " Opt. Mater. Express **6**, 2389 (2016).

[100] T. B. Hoang, G. M. Akselrod, C. Argyropoulos, J. Huang, D. R. Smith, and M. H. Mikkelsen, "Ultrafast spontaneous emission source using plasmonic nanoantennas", Nat. Comm. **6**, 7788 (2015).

[101] G. M. Akselrod, C. Argyropoulos, T. B. Hoang, C. Ciraci, C. Fang, J. Huang, D. R. Smith, and M. H. Mikkelsen, "Probing the mechanisms of large Purcell enhancement in plasmonic nanoantennas", Nat. Photonics **8**, 835 (2014).

[102] C. Guclu, T. S. Luk, G. T. Wang, and F. Capolino,"Radiative emission enhancement using nano-antennas made of hyperbolic metamaterial resonators ", Appl. Phys. Lett. **105**,123101 (2014).

[103] R. Alaee, C. Menzel, U. Huebner, E. Pshenay-Severin, S. Bin Hasan, T. Pertsch, C. Rockstuhl, and F. Lederer, "Deep-Subwavelength Plasmonic Nanoresonators Exploiting Extreme Coupling", Nano Lett. **13**, 3482 (2013).

[104] I. Avrutsky, I. Salakhutdinov, J. Elser, and V. Podolskiy, "Highly confined optical modes in nanoscale metal-dielectric multilayers", Phys. Rev. B **75**, 241402 (2007).

[105] D. R. Smith and D. Schurig, "Electromagnetic Wave Propagation in Media with Indefinite Permittivity and Permeability Tensors", Physical Review Letters **90**, 077405 (2003).

[106] L. Ferrari, C. Wu, D. Lepage, X. Zhang, and Z. Liu, "Hyperbolic metamaterials and their applications", Progress in Quantum Electronics **40**, 1-40 (2015).

[107] Y. Guo, W. Newman, C. L. Cortes, and Z. Jacob, "Applications of Hyperbolic Metamaterial Substrates", Advances in OptoElectronics **2012**, 9 (2012).

[108] V. Caligiuri, R. Dhama, K. V. Sreekanth, G. Strangi, and A. De Luca,"Dielectric singularity in hyperbolic metamaterials: the inversion point of coexisting anisotropies", Scientific Reports **6**, 20002 (2016).

[109] A. A. High, R. C. Devlin, A. Dibos, M. Polking, D. S. Wild, J. Perczel, N. P. de Leon, M. D. Lukin, and H. Park, "Visible-frequency hyperbolic metasurface" Nature **522**, 192 (2015).

[110] N. Vasilantonakis, M. E. Nasir, W. Dickson, G. A. Wurtz, and A. V. Zayats, "Bulk plasmon-polaritons in hyperbolic nanorod metamaterial waveguides", Laser & Photonics Reviews **9**, 345 (2015).

[111] R. Maas, J. van de Groep, and A. Polman, "Planar metal/dielectric single-periodic multilayer ultraviolet flat lens ", Optica **3**, 592 (2016).

[112] E. Centeno and A. Moreau, "Effective properties of superstructured hyperbolic metamaterials: How to beat the diffraction limit at large focal distance", Phys. Rev. B, **92**, 045404 (2015).

[113] C. Long, S. Yin, W. Wang, W. Li, J. Zhu, and J. Guan, "Broadening the absorption bandwidth of metamaterial absorbers by transverse magnetic harmonics of 210 mode", Scientific Reports **6**, 21431(2016).

[114] K. V. Sreekanth, A. De Luca, and G. Strangi, "Experimental demonstration of surface and bulk plasmon polaritons in hypergratings", Scientific Reports **3**, 3291 (2013).

[115] H. Zhu, X. Yin, L. Chen, Z. Zhu, and X. Li, "Manipulating light polarizations with a hyperbolic metamaterial waveguide ", Opt. Lett., **40**, 4595 (2015).

[116] H. Hu, D. Ji, X. Zeng, K. Liu, and Q. Gan, "Rainbow Trapping in Hyperbolic Metamaterial Waveguide", Scientific Reports **3**, 1249 (2013).

[117] S. V. Zhukovsky, O. Kidwai, and J. E. Sipe, "Physical nature of volume plasmon polaritons in hyperbolic metamaterials ", Opt. Express, **21**, 14982 (2013).

[118] T. Taliercio, V. N. Guilengui , L. Cerutti, E. Tournié, J-J. Greffet, "Brewster mode in highly doped semiconductor layers: an all-optical technique to monitor doping concentration", Opt. Express **22**, 24294 (2014).

[119] M. J. Milla, F. Barho, F. Gonzalez-Posada, L. Cerutti, M. Bomers, J. B. Rodriguez, E. Tournié, and T. Taliercio, "Localized surface plasmon resonance frequency tuning in highly doped InAsSb/GaSb one-dimensional nanostructures", Nanotechnology **27**, 425201 (2016).

[120] S. Roux, P. Barritault, O. Lartigue, L. Cerutti, E. Tournié, B. Gerard, and A. Grisard, "Mid-infrared characterization of refractive indices and propagation losses in GaSb/Al_xGa_{1x}AsSb waveguides", Appl. Phys. Lett. **107**, 171901 (2015).

[121] J. Dorfmüller, R. Vogelgesang, W. Khunsin, C. Rockstuhl, C. Etrich, and K. Kern, "Plasmonic Nanowire Antennas: Experiment, Simulation, and Theory", Nano Lett. **10**, 3596 (2010).

[122] T. Kang, W. Choi, I. Yoon, H. Lee, M.-K. Seo, Q.-H. Park, and B. Kim, "Rainbow Radiating Single-Crystal Ag Nanowire Nanoantenna",Nano Lett. **12**, 2331 (2012).

[123] M. Malerba, A. Alabastri, E. Miele, P. Zilio, M. Patrini, D. Bajoni, G. C. Messina, M. Dipalo, T. Sarmiento, R. P. Zaccaria, and F. De Angelis, "3D vertical nanostructures for enhanced infrared plasmonics", Scientific Reports **5**, 16436 (2015).

[124] L.-W. Chou, N. Shin, S. V. Sivaram, and M. A. Filler, "Tunable Mid-Infrared Localized Surface Plasmon Resonances in Silicon Nanowires", j. Am. Chem. Soc. **134**, 16155 (2012).

[125] D. S. Boyuk, L.-W. Chou, and M. A. Filler, "Strong Near-Field Coupling of Plasmonic Resonators Embedded in Si Nanowires", ACS Photonics **3**, 184 (2016).

[126] S. Moumdji, A. Larrue, D. Belharet, P. Dubreuil, S. Bonnefont, O. Gauthier-Lafaye, Y. Rouillard, and A. Vicet, "2.6μm GaSb based photonic crystal coupled cavity lasers", Electron. Lett. **45**, 1119 (2009).

[127] M. Jahjah, S. Moumdji, O. Gauthier-Lafaye, S. Bonnefont, Y. Rouillard, and A. Vicet, "Antimonide-based 2.3 μm photonic crystal coupled-cavity lasers for CH_4", Electron. Lett. **48**, 277 (2012).

[128] Collin, S. Nanostructure arrays in free-space: optical properties and applications. *Rep. Prog. Phys.* **77**, 126402 (2014).

[129] Liu, N., Mesch, M., Weiss, T., Hentschel, M., Giessen, H. Infrared Perfect Absorber and Its Application As Plasmonic Sensor. *Nano Lett.* **10**, 2342–2348 (2010).

[130] Park, H.-R., Chen, X., Nguyen, N.-C., Peraire, J., Oh, S.-H. Nanogap-Enhanced Terahertz Sensing of 1 nm Thick ($\lambda/10^6$) Dielectric Films. *ACS Photonics* **2**, 417–424 (2015).

[131] Shi, C., Zang, X., Wang, Y., Chen, L., Cai,B., Zhu, Y. A polarization-independent broadband terahertz absorber. *Appl. Phys. Lett.* **105**, 031104 (2014).

[132] Hedayati, M., Faupel, F., Elbahri, M. Review of Plasmonic Nanocomposite Metamaterial Absorber. *Materials* **7**, 1221–1248 (2014).

[133] Park, H.-R., Namgung, S., Chen,X., Lindquist, N. C., Giannini, V., Francescato, Y., Maier, S. A., Oh, S.-H. Perfect Extinction of Terahertz Waves in Monolayer Graphene over 2-nm-Wide Metallic Apertures. *Advanced Optical Materials* **3**, 667–673 (2015).

[134] Cui, Y., He, Y., Jin, Y., Ding, F., Yang, L., Ye,Y., Zhong, S., Lin, Y., He, S. Plasmonic and metamaterial structures as electromagnetic absorbers. *Laser and Photonics Reviews* **8**, 495–520 (2014).

[135] Landy, N. I., Sajuyigbe, S., Mock, J. J., Smith, D. R., Padilla, W. J. Perfect Metamaterial Absorber. *Phys. Rev. Lett.* **100**, 207402 (2008).

[136] Behaghel, B., Tamaki, R., Vandamme, N., Watanabe, K., Dupuis, C., Bardou, N., Sodabanlu, H., Cattoni, A., Okada, Y., Sugiyama, M., Collin, S., Guillemoles, J. F. Absorption enhancement through Fabry-Pérot resonant modes in a 430 nm thick InGaAs/GaAsP multiple quantum wells solar cell. *Appl. Phys. Lett.* **106**, 081107 (2015).

[137] Yang, J., Sauvan,C., Jouanin, A., Collin, S., Pelouard, J. L., Lalanne, P. Ultra small metal-insulator-metal nanoresonators: impact of slow-wave effects on the quality factor. *Opt. Express* **20**, 16880–16891 (2012).

[138] Kats, M. A., Blanchard, R., Genevet, P., Capasso, F. Nanometre optical coatings based on strong interference effects in highly absorbing media. *Nat. materials* **11**, 20–24 (2013).

[139] Kats, M. A., Sharma, D., Lin, J., Genevet, P., Blanchard, R., Yang, Z.; Qazilbash, M. M., Basov, D. N., Ramanathan,S., Capasso, F. Ultra-thin perfect absorber employing a tunable phase change material. *Appl. Phys. Lett.* **101**, 221101 (2012).

[140] Yao, Y., Shankar, R., Kats, M. A., Song, Y., Kong, J., Loncar, M., Capasso, F. Electrically Tunable Metasurface Perfect Absorbers for Ultra-thin Mid-Infrared Optical Modulators. *Nano Lett.* **14**, 6526–6532 (2014).

[141] Peng, Y., Zang, X., Zhu, Y., Shi, C., Chen, L., Cai, B. and Zhuang, S. Ultra-broadband terahertz perfect absorber by exciting multi-order

diffractions in a double-layered grating structure. *Opt. Express* **23**, 2032–2039 (2015).

[142] Shi, C., Zang, X. F., Chen, L., Peng, Y., Cai, B., Nash, G. R. and Zhu, Y. M. Compact Broadband Terahertz Perfect Absorber Based on Multi-Interference and Diffraction Effects. *IEEE Trans. Terahertz science and technology* **6**, 40–44 (2016).

[143] Zang, X., Shi, C., Chen, L., Cai, B., Zhu, Y. and Zhuang, S. Ultra-broadband terahertz absorption by exciting the orthogonal diffraction in dumbbell-shaped gratings. scientific Reports **5**, 8901 (2015).

[144] Collin, S., Pardo, F., Pelouard, J.-L. Waveguiding in nanoscale metallic apertures. *Opt. Express* **15**, 4310–4320 (2007).

[145] Garcia-Vidal, F. J., Martin-Moreno, L., Ebbesen, T. W., Kuipers, L. Light passing through subwavelength apertures. *Rev. Mod. Phys.* **82**, 729–787 (2010).

[146] Moreau, A., Lafarge, C., Laurent, N., Edee, K., Granet, G. Enhanced transmission of slit arrays in an extremely thin metallic film. *J Opt. A: Pure Applied Optics* **9**, 165–169 (2007).

[147] Koechlin, C., Bouchon, P., Pardo, F., Pelouard, J.-L., Haidar, R. Analytical description of subwavelength plasmonic MIM resonators and of their combination. *Opt. Express* **21**, 7025–7032 (2013).

[148] Benedicto J., Centeno E., Pollès R., and Moreau A. Ultimate resolution of indefinite metamaterial flat lenses, Phys. Rev. B **88**, 245138 (2013).

[149] Benedicto J., Centeno E., and Moreau A. Lens equation for flat lenses made with hyperbolic metamaterials, Opt. Lett., **37**, 4786 (2012).

[150] Kidwai, O., Zhukovsky, S. V. and Sipe, J. E. Effective-medium approach to planar multilayer hyperbolic metamaterials: Strengths and limitations. *Phys. Rev. A* **85**, 053842 (2012).

[151] Etrich, C., Fahr, S., Hedayati, M., Faupel, F., Elbahri, M. and Rockstuhl, C. Effective Optical Properties of Plasmonic Nanocomposites. *Materials* **7**, 727–741 (2014).

[152] Shen, J. T., Catrysse, P. B. and Fan, S. Mechanism for Designing Metallic Metamaterials with a High Index of Refraction. *Phys. Rev. Lett.* **94**, 197401 (2005).

[153] Palik, E.D. "Handbook of Optical constants of solids," *Academic Press Inc.*, New York **1991**.

[154] K. Fan, W.-J. Padilla, "Dynamic electromagnetic metamterials," Materials Today **18** (2015)

[155] F. Omeis, R. Smaali, F. Gonzalez-Posada, L. Cerutti, T. Taliercio, and E. Centeno, "Metal-insulator-metal antennas in the far-infrared range based on highly doped InAsSb." *Appl. Phys. Lett.* **111** (2017)